



University of
Massachusetts
Amherst

Constraining The Metallicity Of The Low-density Ly Alpha Forest Using O Vi Absorption

| | |
|---------------|---|
| Item Type | Article |
| Authors | Dave, R;Hellsten, U;Hernquist, L;Katz, N;Weinberg, DH |
| DOI | 10.1086/306524 |
| Download date | 2026-03-07 08:38:33 |
| Link to Item | https://hdl.handle.net/20.500.14394/3029 |

Constraining the Metallicity of the Low Density Lyman-Alpha Forest Using OVI Absorption

Romeel Davé, Uffe Hellsten and Lars Hernquist

Astronomy Department, University of California, Santa Cruz, CA 95064

Neal Katz

Astronomy Department, University of Massachusetts, Amherst, MA 01003

and

David H. Weinberg

Astronomy Department, Ohio State University, Columbus, OH 43210

ABSTRACT

We present a systematic search for OVI(1032Å,1037Å) absorption in a Keck HIRES spectrum of the $z = 3.62$ quasar Q1422+231, with the goal of constraining the metallicity and ionization state of the low density intergalactic medium (IGM). Comparison of CIV absorption measurements to models of the Ly α forest based on cosmological simulations shows that absorbers with $N_{\text{HI}} \gtrsim 10^{14.5} \text{cm}^{-2}$ have a mean carbon abundance $[\text{C}/\text{H}] \approx -2.5$, assuming a metagalactic photoionizing background with the spectral shape predicted by Haardt & Madau (1996, HM). In these models, lower column density absorption arises in lower density gas where most CIV is photoionized to CV. Therefore, OVI should be the most sensitive tracer of metallicity in Ly α absorbers with $N_{\text{HI}} \lesssim 10^{14.5} \text{cm}^{-2}$. OVI lines lie at wavelengths heavily contaminated by Lyman series absorption, so we interpret the search results by comparing to carefully constructed, mock Q1422 spectra drawn from a hydrodynamic simulation of a Λ -dominated cold dark matter model.

A search for deep, narrow absorption features yields only a few candidate OVI lines in the spectrum of Q1422. HI absorption blankets the position of the doublet companion line in each case, and the total number of narrow lines is statistically consistent with that in zero-metallicity artificial spectra. Artificial spectra generated with the HM background and $[\text{O}/\text{H}] \gtrsim -2.5$ predict too many narrow lines and are statistically inconsistent with the data. We also search for OVI associated with CIV systems, using the optical depth ratio technique of Songaila (1998). With this method we *do* find significant OVI absorption; matching the data requires $[\text{O}/\text{C}] \approx +0.5$ and corresponding $[\text{O}/\text{H}] \approx -2.0$. Taken together, the narrow line and optical depth ratio results imply that (a) the metallicity in the low density regions of the IGM is at least a

factor of three below that in the overdense regions where CIV absorption is detectable, and (b) oxygen is overabundant in the CIV regions, consistent with the predictions of Type II supernova enrichment models and the observed abundance pattern in old halo stars.

The photoionizing background spectrum would be truncated above 4 Ry in regions that have not undergone helium reionization (HeII \rightarrow HeIII), and in this case matching the Q1422 data requires lower [C/H] but higher [O/H]. Taking [O/C] \approx +1 as the maximum plausible overabundance of oxygen, we conclude that helium must have been reionized through at least 50% of the volume from $z \sim 3 - 3.6$.

Subject headings: galaxies: formation — intergalactic medium — line: identification — methods: numerical — quasars: absorption lines — quasar: individual (1422+231 = B 1422+231)

1. Introduction

The Lyman alpha ($\text{Ly}\alpha$) “forest” (Lynds 1971; Sargent et al. 1980) of spectral features caused by HI absorption along the line of sight to a quasar probes the state of the intergalactic medium over a wide range of physical conditions. During the past few years, high-precision observations made using the HIRES spectrograph (Vogt et al. 1994) on the 10m Keck telescope have quantified the statistics of these low column density absorbers to unprecedented accuracy (e.g., Hu et al. 1995; Lu et al. 1996b; Kim et al. 1997; Kirkman & Tytler 1998). During the same time span, cosmological simulations that incorporate gas dynamics, radiative cooling, and photoionization have been able to reproduce many of the observed properties of quasar absorption spectra (Cen et al. 1994; Zhang, Anninos & Norman 1995; Hernquist et al. 1996; Miralda-Escudé et al. 1996; Davé et al. 1997). The rapid progress on theoretical and observational fronts has led to the emergence of a new paradigm for the origin of the high-redshift ($z \gtrsim 2$) $\text{Ly}\alpha$ forest, in which most $\text{Ly}\alpha$ forest lines are produced by regions of low to moderate overdensity in hierarchically collapsing structures that are not in dynamical or thermal equilibrium. $\text{Ly}\alpha$ lines of lower column density generally arise in gas of lower physical density, which has a lower neutral hydrogen fraction because of the reduced recombination rate. In this paper, we use a matched comparison between a cosmological hydrodynamic simulation and a Keck HIRES spectrum of the quasar Q1422+231 to constrain the metal abundance of this low density gas.

The recent detection of metal lines associated with $\text{Ly}\alpha$ forest absorbers having column densities $N_{\text{HI}} \lesssim 10^{15} \text{cm}^{-2}$ (Cowie et al. 1995; Tytler et al. 1995; Songaila & Cowie 1996, hereafter SC96) has provided a new avenue for investigating the ionization state and enrichment history of the high-redshift intergalactic medium (IGM). SC96 showed that 75% of $\text{Ly}\alpha$ absorbers with $N_{\text{HI}} > 10^{14.5} \text{cm}^{-2}$ have associated CIV absorption. Using simple photoionization models they

estimate that the mean metallicity of these absorbers is between¹ $[C/H] \sim -2$ and -3 . Studies that use cosmological simulations to model the density and temperature of the absorbing gas obtain a better match to the data for a mean metallicity of $[C/H] \sim -2.5$ with around one dex of scatter, assuming either a power-law ionizing background (Haehnelt, Steinmetz, & Rauch 1996) or a reprocessed quasar ionizing background (Hellsten et al. 1997, hereafter HDHWK).

The question of how metals came to reside in these intermediate-density Ly α absorbers remains unanswered. Since Ly α absorbers with $N_{\text{HI}} \lesssim 10^{15} \text{cm}^{-2}$ are optically thin and associated with density peaks of overdensity $\lesssim 20$, it is unlikely that they contain star-forming regions that produce *in situ* enrichment. Thus some transport mechanism must be invoked to explain the presence of metals in these regions. One possibility is that the metals are ejected from nearby, forming galaxies, by some combination of supernova blowout (Miralda-Escudé & Rees 1998) and tidal stripping (Gnedin & Ostriker 1997; Gnedin 1998). Since the enriching proto-galaxies are likely to form more efficiently in high density environments, these scenarios predict a significant correlation between metallicity and density (see, e.g., figure 6 of Gnedin & Ostriker 1997). Alternatively, the IGM may have been enriched at a very early epoch by more ubiquitous Population III objects (e.g., Haiman & Loeb 1997), in which case all Ly α absorbers might be expected to have roughly the same metallicity. Because CIV lines probe only a small range of HI column densities (and hence physical densities) with adequate statistics, it is difficult to distinguish between these enrichment models using only CIV data. Metal abundances can be studied at higher densities in Lyman limit systems ($N_{\text{HI}} \gtrsim 10^{17} \text{cm}^{-2}$) and damped Ly α systems ($N_{\text{HI}} \gtrsim 10^{20} \text{cm}^{-2}$), but these are objects where *in situ* enrichment is likely and where (especially for Lyman limit systems) uncertain radiative transfer effects complicate the inference of metal abundances from line strengths.

In this paper, we attempt to extend metallicity constraints to the low column density ($N_{\text{HI}} \lesssim 10^{14.5} \text{cm}^{-2}$), and hence low physical density, Ly α forest. Carbon is difficult to detect in this regime because the low density reduces N_C and ionizes more CIV to CV. However, Lu et al. (1998) have used composite spectra to attempt to detect CIV in such systems, and we briefly discuss their results in §8. In this paper, we focus instead on OVI, which is expected to be the one detectable metal absorption feature tracing Ly α absorbers with $N_{\text{HI}} \lesssim 10^{14.5} \text{cm}^{-2}$ because of its high ionization state and large oscillator strength (Hellsten et al. 1998, hereafter HHKW). The difficulty with this approach, and the reason that it has not been previously attempted, is that the OVI absorption features lie embedded within the Ly α forest, which is quite crowded at these redshifts. We overcome this problem by using a line identification scheme specifically designed to select candidate OVI features and by using artificial spectra extracted from a realistic cosmological simulation to calibrate the efficiency of OVI detection and the contamination from narrow Ly α lines. With these procedures, we can test whether the low density regions of the Ly α forest are consistent with a uniform metallicity extrapolated from the CIV data at higher densities.

¹We use the standard notation of brackets to denote the relative abundance, in logarithm, versus solar.

The low density IGM is highly photoionized by the metagalactic ultraviolet (UV) background. For our standard spectral shape, we assume that the UV background is produced by quasar emission reprocessed by Ly α forest absorption (Haardt & Madau 1996, hereafter HM). We find that if the IGM metallicity is uniform at $[C/H] \sim -2.5$, the UV background has the spectral shape given by HM, and oxygen has the factor of three overabundance (relative to solar) predicted by Type II supernova enrichment models, then OVI should be readily detectable in the spectrum of Q1422+231. However, our detection algorithm finds very few candidate OVI lines in the spectrum. The absence of detectable OVI features has several possible interpretations: (1) oxygen is not overabundant relative to carbon in the low density IGM, (2) the metallicity of low density regions as traced by $N_{\text{HI}} \lesssim 10^{14.5} \text{cm}^{-2}$ Ly α absorption systems is lower than the metallicity of intermediate-density regions traced by higher column density absorption, or (3) there are many fewer high-energy photons capable of photoionizing OV to OVI than are predicted by the HM ionizing background.

To distinguish between these interpretations, we apply a second algorithm, the optical depth ratio technique of Songaila (1998, hereafter S98) designed to detect OVI in regions where significant CIV absorption is found. Since we have independently determined $[C/H]$ in these regions, we can use this technique to discriminate between different ionization conditions and abundance patterns. By applying this technique to the spectrum of Q1422+231 and calibrating the results using artificial spectra, we find that: (1) a significant metallicity gradient (declining metallicity with declining density) must exist regardless of whether helium has mostly reionized or not, (2) if helium has reionized by $z \sim 3.6$, our results are consistent with $[O/C] \approx +0.5$, and (3) if the epoch of helium reionization does not begin until $z \sim 3$, a highly implausible oxygen overabundance of $[O/C] \gtrsim +2$ is required.

Combining the results from these two analysis techniques, our favored scenario for the low density IGM at $z \gtrsim 3$ is one in which more than half of the volume of the universe has helium predominantly reionized by $z \sim 3.6$, oxygen is overabundant relative to carbon by a factor $\gtrsim 3$, and spatial regions with overdensities ~ 10 have an average metallicity *at least* a factor of 3 higher than regions near the mean baryonic density.

Section 2 describes our cosmological simulation, the Q1422+231 data, and our procedure for constructing artificial absorption spectra. Section 3 discusses previous OVI searches and reviews HHKW’s argument that OVI should be the most effective tracer of metallicity in Ly α absorbers with $N_{\text{HI}} \lesssim 10^{14} \text{cm}^{-2}$. Section 4 examines CIV absorption at intermediate column densities, repeating the general arguments of HDHWK and Rauch et al. (1997a) but with a much closer match between the theoretical and observational analysis procedures. Section 5 is the heart of the paper. It describes our algorithm for identifying candidate OVI lines, presents the results of the OVI searches in the real and artificial spectra, and discusses the properties of candidate OVI absorbers in Q1422+231 and the simulations. Figures 5–7 demonstrate the paper’s central results. Section 6 discusses the impact of varying the assumptions of our standard theoretical model. Section 7 describes the optical depth ratio technique for quantifying OVI absorption,

shows the results from this technique applied to Q1422+231 and artificial spectra, and discusses these results in conjunction with the results from Section 5. Section 8 summarizes our conclusions and discusses them in light of other recent observational and theoretical developments.

2. Modeling the Lyman Alpha Forest

2.1. Simulation

We perform a cosmological hydrodynamic simulation of a Λ -dominated cold dark matter (LCDM) model with $\Omega_\Lambda = 0.6$, $\Omega_{\text{CDM}} = 0.3527$, $\Omega_b = 0.0473$, $H_0 = 65 \text{ km s}^{-1} \text{ Mpc}^{-1}$, inflationary spectral index $n = 0.95$, and rms fluctuation amplitude $\sigma_8 = 0.8$. These values yield a COBE-normalized LCDM model that is in agreement with most current observational constraints (Miralda-Escudé et al. 1996). We chose the LCDM model because it reproduces the characteristics of the Ly α forest of Q1422+231 most closely (Davé et al. , in preparation), although the differences from other popular cosmologies are slight. We choose the value of the baryon density Ω_b to match recent observations of the deuterium abundance that give $\Omega_b \approx 0.02h^{-2}$ (Burles & Tytler 1998a; Burles & Tytler 1998b). Matching the observed mean transmission in the Ly α forest using reasonable estimates for the intensity of the metagalactic photoionizing background also requires a baryon abundance of this order (Hernquist et al. 1996; Rauch et al. 1997b; Weinberg et al. 1997).

The simulations were performed using PTreeSPH (Davé, Dubinski & Hernquist 1997), a version of the TreeSPH code (Hernquist & Katz 1989; Katz, Weinberg & Hernquist 1996) implemented on massively parallel supercomputers. We use 64^3 dark matter particles and 64^3 gas particles in a periodic cube $11.111h^{-1}$ comoving Mpc on a side and a gravitational softening length of $3h^{-1}$ comoving kpc (equivalent Plummer softening). The masses of the dark matter and gas particles are $9.64 \times 10^8 M_\odot$ and $1.37 \times 10^8 M_\odot$, respectively. The initial fluctuations are a Gaussian random field with the power spectrum computed using the Hu & Sugiyama (1996) formulation of the CDM transfer function. We include radiative cooling for primordial composition gas and photoionization and heating from a spatially uniform UV background. We adopt the UV spectral shape and intensity (versus redshift) from HM, with the exception that the intrinsic quasar spectrum has been softened from a power law index of -1.5 to -1.8 , as is now favored by those authors (Madau, private communication); we shall still refer to this as the HM spectrum. We compute the relative abundances of ionic species assuming equilibrium between ionization and recombination (see Katz, Weinberg & Hernquist 1996); we will examine possible effects of this assumption in §6.2. We include a prescription for star formation, but for the results contained in this paper, this has no significant effect (Weinberg et al. 1996). We ran from a starting redshift of $z = 49$ to $z = 2$. This simulation took roughly 3400 node-hours on 16 processors of the Cray T3E at the Pittsburgh Supercomputing Center.

2.2. Spectrum of Quasar Q1422+231

In this paper we will be comparing our simulations to only one quasar spectrum, that of Q1422+231² (shown in the upper left panel of Figure 1), since that is the only one currently available to us. It was generously provided to us by A. Songaila and L. Cowie, and their observations of Q1422 using Keck’s HIRES spectrograph are described more fully in SC96. Here we briefly note that the quasar emission redshift is $z = 3.62$, and the spectral resolution (as provided to us) is 0.06\AA , corresponding to roughly $4.5 - 3.2 \text{ km s}^{-1}$ per pixel from 3900\AA to 7200\AA . The signal-to-noise ratio is roughly $30 - 40$ per pixel in the region of $\text{Ly}\beta$ and OVI absorption ($\lambda \lesssim 4800\text{\AA}$), $50 - 60$ per pixel in the pure $\text{Ly}\alpha$ forest region, and over 100 per pixel in the metal line region redwards of the $\text{Ly}\alpha$ emission peak. Due to a Lyman limit system at $z = 3.3816$, the spectrum of Q1422 effectively truncates around 4000\AA . Thus $\lambda \sim 4000\text{\AA} - 4800\text{\AA}$ represents the usable region for our OVI search, corresponding to $z \sim 2.9 - 3.6$, with poorer sensitivity towards lower redshifts because of the dropping intrinsic flux of the quasar and the degrading response of HIRES towards the blue.

2.3. Continuous Artificial Spectra

To model Q1422 as closely as possible, we have developed a new method for generating artificial quasar spectra from a cosmological simulation. Our approach produces continuous line-of-sight artificial spectra between two desired wavelengths, analogous to real quasar spectra, rather than a large number of small, disjoint spectra at a single redshift as has been typically done in other studies (e.g., Hernquist et al. 1996). The advantages of these *continuous artificial spectra* are that they automatically include the redshift evolution intrinsic to any given model and that the similarity between the artificial spectra and the real quasar spectrum allows the identical analysis routines to be applied to both. This reduces the algorithm-dependent variations of continuum fitting, noise estimation, and most importantly for this work, metal line identification.

Generating continuous spectra requires that particle information be output at frequent intervals during a simulation. Since we cannot output all the simulation data every few timesteps owing to disk space and I/O time constraints, we output only the particle information required to generate the desired spectra. We choose the frequency of output data so that the redshift interval between outputs exactly equals the length of the box in redshift space, given by

$$\Delta z = LH(z)/c = 3.33 \times 10^{-4} [H(z)/H_0] L, \quad (1)$$

where $H(z)$ is the Hubble constant at redshift z , H_0 is the Hubble constant today, L is the simulation size in comoving $h^{-1}\text{Mpc}$, and c is the speed of light. At each output timestep during the simulation run, we choose six random lines of sight from within the volume. We output

²Hereafter, we will refer to Q1422+231 as “Q1422”.

information (i.e. $m, \mathbf{x}, \mathbf{v}, T, \rho, h_{\text{smooth}}$) for all gas particles whose SPH smoothing volume (i.e., the region of space a gas particle represents) intersects one of these lines of sight. At each output, a new set of six lines of sight is randomly chosen. We begin outputting spectra continuously at $z = 4.2$; roughly 100 outputs are required to $z = 2$.

We use this particle information together with the assumed ionizing background interpolated to the output redshift to generate optical depths along these lines of sight for the following ions: HI, HeI, HeII, CIV, CII, SiIV, NV, and OVI. We use CLOUDY 90 (Ferland 1996) to compute lookup tables for the fraction of gas in each ionization state at a given density and temperature for our adopted J_ν , accounting for both photoionization and collisional ionization, and we use routines extracted from the TIPS package (Katz & Quinn 1995) to compute smoothed gas properties along each line of sight; see HDHWK for more details. We assume that the gas is optically thin, which is appropriate for the Ly α forest regime. We compute the profiles of optical depth versus observed wavelength (or, equivalently, versus redshift) individually for each output box, then join the contiguous output boxes to produce continuous spectra for redshifts below $z = 4.2$ along each of the six lines of sight.

When producing these continuous spectra, we have to pay special attention to the regions where the spectra from contiguous output boxes are joined, because the physical properties there are discontinuous. Since the simulation volume is periodic, we can arbitrarily shift the particle positions, and hence the computed optical depths, in a periodic sense within a single output box. We shift the optical depths so that the point of lowest HI absorption lies at the ends of the spectra at any given output. Thus we join the spectra in regions of very low optical depth, which for our purposes are uninteresting; they also arise from voids that have relatively smooth and homogeneous physical properties. We smooth these transition regions over a small interval of five pixels out of a total of 1000 output pixels (where one pixel in our artificial spectrum corresponds to $\sim 1.5 \text{ km s}^{-1}$ at these redshifts).

With a list of optical depths versus redshift for various ions, we are now equipped to produce artificial quasar spectra. We select a quasar spectrum to simulate (in our case Q1422), specifying its redshift, the wavelength interval over which we wish to produce a spectrum, its resolution in wavelength space, and a spatially uniform metallicity. We assume an abundance pattern typical of low-metallicity stars and HII regions, presumably enriched by Type II supernovae: $Z \equiv [\text{Fe}/\text{H}] = [\text{C}/\text{H}]$, $[\text{N}/\text{C}] = -0.7$, $[\text{Si}/\text{C}] = +0.4$, and $[\text{O}/\text{C}] = +0.5$; we discuss these ratios further in §6.1. In each wavelength bin, we sum the contribution to the optical depth from all ions with redshifts lower than the quasar redshift. We consider the entire Lyman series up to Ly-30, and both doublet components for the metal species. This procedure yields a list of “observed” optical depths versus wavelength at the specified spectral resolution.

We now add noise and fit a continuum to each artificial spectrum. Although we know the true location of the continuum in advance, it is important to perform a continuum fit to maintain equivalence between the procedures for analyzing observed and artificial spectra. We

have developed automated routines for estimating the signal-to-noise ratio on a pixel-by-pixel basis and fitting a continuum to raw quasar data. We estimate the noise by first identifying small regions of saturation and measuring the average detector noise, and then finding regions of “continuum” to estimate the average noise from photon statistics, within 30\AA segments of the spectrum. In the dense Ly α forest it is difficult to find sizable regions where the flux is near the continuum, so typically the shot noise is somewhat overestimated because it includes a contribution from fluctuating low level absorption. We have not corrected for this effect. Nevertheless, our noise estimates agree reasonably well with those of SC96. We estimate the continuum by fitting smoothed second-order polynomials to the spectral peaks in 30\AA intervals. While this may appear crude, no method can recover the true continuum because even in the artificial spectra the flux rarely approaches the true continuum level for $z \gtrsim 3$. Thus we strive only to implement a method that can be applied identically to the real and artificial spectra, is similar to methods traditionally used in observational analyses, and uses a low order fitting function in order to minimize “overfitting” of true absorption fluctuations. Because our OVI search below is based on identification of narrow isolated absorption features, the details of continuum fitting are not critical for our current purposes.

We estimate the continuum and noise characteristics of Q1422 using the above algorithms. To incorporate noise into the artificial spectra, we take the detector noise and shot noise as estimated in the observed spectra and add it directly (with a Gaussian random distribution) to the intensity of the artificial spectra, giving the artificial spectra very similar noise characteristics to the observed spectra. We continuum fit the artificial spectra, and the resulting data are output as a single artificial quasar spectrum.

The intensity of the metagalactic photoionizing background (J_ν) is not tightly constrained by current observations. We use the intensity predicted by HM when evolving the simulation, but because J_ν does not significantly affect the dynamics in the optically thin, low-to-moderate overdensity regions, we can vary the intensity of J_ν *a posteriori* to desired levels and obtain nearly identical results to having redone the entire simulation with that J_ν (Weinberg et al. 1997). To constrain J_ν , we note that the mean opacity $\langle e^{-\tau} \rangle$ of the Ly α forest depends on the parameter combination Ω_b^2/J_ν , since the HI optical depths are proportional to this combination (for fixed gas temperature). After obtaining a noise-added, continuum-fitted artificial spectrum, we measure its mean transmission, then use that information to adjust J_ν , and repeat the above procedure to produce a new quasar spectrum. We typically iterate several times until the mean transmission converges to within 1% of the observed mean transmission for Q1422; this corresponds to a determination of J_ν to better than 2% (given our adopted Ω_b). We perform this process individually for each artificial quasar spectrum. For our LCDM model, the average factor by which the HM intensity must be increased is 1.29 ± 0.18 , where the variance is computed over the six artificial spectra. As a side note, the implied value of Ω_b for consistency with the HM intensity itself is $0.0176 \pm 0.0011h^{-2}$ for this model.

Once we have an intensity of J_ν for each artificial spectrum, we now recalculate the metal

species’ optical depths using this new intensity, because unlike HI absorption, metal absorption does not scale in a trivial way with J_ν . Once we calculate the new optical depths, we again fit a continuum and add noise in the manner described above. Therefore, each artificial spectrum has the correct HI mean transmission, and the metal absorption is computed assuming a spatially uniform metallicity and ionizing background with the HM shape and an intensity constrained by the mean transmission of Q1422.

In Figure 1 (left panels) we show the spectrum of Q1422 (reproduced from SC96) and an example of one of our six artificial spectra for Q1422 with metallicity $Z = -2.5$, with the corresponding continuum fit and noise level (multiplied by four for visibility) in the Ly α forest region. The differences between these two spectra are due to: (1) emission features in the quasar not present in the artificial spectra, (2) the downward slope of the observed continuum in the Ly α forest of Q1422 caused by the intrinsically varying spectral intensity of the quasar and the declining response of the HIRES spectrograph towards the blue, and (3) the intrinsic fluctuations in the continuum level of Q1422. These features in Q1422 are subsequently normalized out by fitting a continuum level to the peaks, as shown in the upper right panel of Figure 1; the identical continuum fitting routine is applied to the artificial spectrum for consistency. After this procedure, the artificial spectrum contains all the significant characteristics of the Q1422 spectrum, as shown in the lower right panel of Figure 1. We also fit a continuum to the spectra redwards of the Ly α peak; this procedure is much more robust since there are plenty of regions of virtually unabsorbed continuum.

There are some features of real quasar spectra that are not reproduced in these continuous artificial spectra, although we expect that these differences will not significantly affect our results. First, correlations of lines across the boundaries where the segmented spectra have been joined are not properly reproduced; thus caution must be taken when using these spectra to measure line-of-sight correlation functions. In this paper, we are counting and measuring only isolated lines, so this problem does not arise. Second, metal line absorption from systems at low redshift is not properly taken into account, since our artificial spectra stop at $z = 2$. In practice, the influence of interloping metal lines on the mean transmission in the Ly α forest region is extremely small, so our determination of J_ν is virtually unaffected. Third, real spectra have intrinsic small-scale variations in their noise level, e.g., owing to a fluctuating response across an Echelle order. The noise level of the artificial spectra is constant over a $\sim 30\text{\AA}$ scale, so these small-scale fluctuations are not reproduced. We do not expect this to have a significant effect on our conclusions, but in future work we will model some of these effects in greater detail.

3. Previous Searches for OVI

Previous searches for OVI absorption at high redshifts have had very limited success. The only claimed detection of an OVI line at $z \gtrsim 2$ is by Kirkman & Tytler (1997; hereafter KT97). They found a single narrow feature in Q1422 which they identified as OVI primarily on the basis

of associated CIV absorption. The doublet companion was subsumed by an HI line.

The method of searching for OVI associated with CIV is taken from low-redshift studies (Lu 1991; Burles & Tytler 1996). However, given a universe with a homogeneous metallicity and an ionizing background shape similar to that predicted by HM, this strategy is not the optimal way to find OVI. The reason for this is illustrated by the Line Observability Index (LOX) plot in Figure 2.

The LOX is described more fully in HHKW; here we outline the relevant features. The LOX is calculated using the density-temperature relation taken from a balance between cosmic expansion and photoionization heating, which predicts $T \propto \rho^{0.7}$, and the peak density-column density relation computed from artificial spectra,

$$\log n_{\text{H}} = -14.7 + \log \frac{\Omega_b h^2}{0.02} + 0.7 \log N_{\text{HI}}. \quad (2)$$

Using these relations, a given HI column density can be associated with a particular ionization condition, from which the fraction in any ionization state can be calculated using CLOUDY 90 (Ferland 1996). Combined with an assumed (uniform) metallicity, here taken to be $10^{-2.5}$ solar for CIV and 10^{-2} solar for OVI, this analysis predicts a rest equivalent width $W_{r\lambda}$ for a typical absorption line of a given species. By the appropriate choice of additive constants (see HHKW), the LOX is given by

$$\text{LOX} \approx \log(W_{r\lambda}/1\text{m}\text{\AA}), \quad (3)$$

where the equation is exact in the limit of weak lines.

Figure 2 shows the LOX of OVI and CIV given the HM spectrum (solid curves). The horizontal dot-dashed line corresponds roughly to the detectability limit in the Ly α forest of Q1422, while the horizontal dotted line reflects the detectability limit redwards of the Ly α emission peak. The dashed curves will be addressed in §6.3. This figure is similar to Figures 3–5 of HHKW except that the LOX is now calculated for the LCDM model used in this paper, which has a higher baryon fraction. The impact of the higher Ω_b is minimal, as HHKW predicted it would be.

As stated in HHKW, given the assumed metallicity and ionization state, CIV will be observable in lines with HI column densities $N_{\text{HI}} \gtrsim 10^{14}\text{cm}^{-2}$, while OVI will be observable to significantly lower HI column densities, down to almost 10^{13}cm^{-2} (if the OVI line is not subsumed by an HI line). Since the column density distribution $d^2N/dN_{\text{HI}}dz \propto N_{\text{HI}}^{-1.7}$ (e.g. Hu et al. 1995; Davé 1998), there are many more HI lines at lower column densities. This means that in any given quasar spectrum, if the metallicity is uniform across all HI column densities, photoionized OVI should be associated with HI lines that often have no associated CIV absorption. We demonstrate this point more quantitatively in §5.3 below.

KT97 claimed that the OVI detected in their $z = 3.3816$ Lyman limit system in Q1422 must be collisionally ionized, in part by arguing that few high-energy photons capable of ionizing oxygen to OVI would exist far from quasars. They argued that while HM assumed uniform emissivity

of quasars, in reality quasars are discrete sources, and far from quasars there should be further softening of the radiation field due to reprocessing by ambient HeII. They calculated the mean free path of HeII-ionizing (4 Ry) photons to be roughly $5h^{-1}\text{Mpc}$, and from this value obtained a volume filling factor of only 2%.

While valid for HeII, the extension of this argument to OVI is less certain. Photons capable of ionizing OV to OVI require energies greater than $114\text{ eV} \approx 8.4\text{ Ry}$. Since the cross section of absorption scales as ν^{-3} , the mean free path of an OV ionizing photon is $(8.4/4)^3 \approx 10$ times that of an HeII ionizing photon. Given this additional factor of about 1000 in volume, a universe with the observed distribution of quasars and a HM ionizing background will effectively be transparent to OV-ionizing photons. This does not imply that the OVI absorption system detected by KT97 is necessarily photoionized — it is associated with a high column density HI absorber that might well be embedded in a collapsed gas halo hot enough to cause collisional ionization. Nevertheless, while our assumption of a uniform ionizing background may be an oversimplification, we do not expect that its spectrum should have *systematically* fewer OV-ionizing photons than predicted by HM, provided that most HeII has been reionized to HeIII by the redshift in question.

4. Metallicity of the Intermediate Density Ly α Forest

4.1. Identifying and Fitting CIV lines

In HDHWK we analyzed CIV artificial spectra in a manner similar to SC96’s procedure, allowing a direct comparison with SC96’s results. However, the artificial spectra used were of the “segment spectra” variety, i.e. , many small intervals of spectra at particular redshifts, and the detailed modeling of Q1422 was not as sophisticated as we do here. In this section, we describe a reanalysis of CIV absorption in Q1422, alongside an analysis of CIV in our continuous artificial spectra. The main additional ingredient is that we now identify and fit CIV and HI absorption features in the artificial spectra and Q1422 using the same routines. Nevertheless, the basic results are similar to those of HDHWK.

The automated Voigt profile fitter AutoVP (Davé et al. 1997) has been extended to identify and fit metal line doublets lying outside the Ly α forest, such as CIV. Once a spectrum has been fitted with Ly α lines, the identification scheme searches for spectral features in the Ly α forest region where the intensity drops below some threshold, taken to be 0.7. Within the wavelength interval where the intensity is below that threshold, AutoVP searches for associated CIV absorption in the two regions corresponding to the doublet positions. If an absorption feature is due to CIV, it should be present in both regions, with the strong component region (1548Å) having twice the optical depth of the weak component region (1551Å) because of the difference in oscillator strengths. To identify any absorption that could possibly be CIV, AutoVP doubles the optical depths of each pixel in the weak component region, superimposes them on the strong line region with an appropriate shift in wavelength, then takes the smaller of the two optical depths

(strong component or double the weak component) as its measure of CIV absorption. Since CIV is the dominant species of absorption redwards of the Ly α emission peak, the implicit assumption that all absorption identified in this way is CIV turns out to be quite good³. We then fit this remaining absorption with CIV Voigt profiles, and sum the column densities within the region.

The associated HI column density is found by summing all column densities of HI lines within the associated spectral region. Since the Ly α feature is typically saturated and therefore yields an inaccurate estimate of the HI column density, AutoVP searches down the Lyman series until it finds the first non-saturated Lyman series region, or alternatively the last observable Lyman series region before the blue cutoff in the spectrum; this is the HI line which is fit. Wherever possible, the unsaturated regions of other Lyman series lines (except Ly α) are converted to optical depths, and used to constrain the optical depth at the associated position in the fitted Lyman series line region; this minimizes the contribution due to coincident absorption from other Lyman series lines. After this constraint has been applied, the Lyman series region is fit with Voigt profiles to obtain the HI column density. Often each region has several HI and CIV lines; we do not attempt to associate individual CIV lines with HI lines, as varying ionization conditions and bulk motions can make this identification very confusing and produce unphysical results. Our procedure is similar to that of SC96, although they fit all Lyman series lines simultaneously to obtain the HI column density. In any case, we apply the exact same detection and measurement algorithm to Q1422 and the artificial spectra, so whatever biases are introduced will be similar in both data sets.

4.2. CIV/HI

Figure 3 shows our reanalysis of CIV lines in Q1422 and an identical analysis of our six artificial Q1422 spectra assuming a uniform metallicity of $[C/H] = -2.5$. The identified CIV systems in Q1422 correspond reasonably well with SC96’s systems; the main differences arise from the estimate of N_{HI} . We conclude that our procedure is not markedly different in practice from that of SC96.

The scatter in the CIV/HI ratio at a given column density in the simulated spectra arises from spatial variations in the density and temperature and from variations introduced by line identification and fitting. The ionizing background and metallicity are assumed to be spatially uniform. The assumed metallicity of $[C/H] = -2.5$ yields a mean CIV/HI ratio in good agreement with Q1422, as we show in Figure 4. Rauch et al. (1997a) and HDHWK found that a 1 dex scatter in metallicity was required for simulations to reproduce the observed scatter in CIV/HI. Our more closely matched comparison here implies a smaller intrinsic scatter of about 0.5 dex; the reduction arises mainly because of additional “observational” scatter introduced by the line fitting

³It is even a reasonable assumption for SiIV and NV, as the metal line region is typically sparse enough that coincident absorption is rare.

algorithm.

We determine the metallicity required to match the mean value of CIV/HI by varying the assumed metallicity and then identifying and fitting metal lines in the artificial spectra. Figure 4 (solid curve) shows the mean log column density of observed CIV lines ($\langle \log N_{\text{CIV}} \rangle$) as a function of metallicity. We find $\langle \log N_{\text{CIV}} \rangle$ to be the most robust statistic for this comparison. Similar results are obtained by using the fraction of HI lines with detectable CIV or the median value of CIV/HI. The solid horizontal line is $\langle \log N_{\text{CIV}} \rangle$ for Q1422’s CIV systems, identified by the same method that was applied to the artificial spectra. The crossover is seen to occur right around $[\text{C}/\text{H}] = -2.5$ (slightly higher if the median CIV/HI is used). The errorbars indicate the variance of $\langle \log N_{\text{CIV}} \rangle$ over the six artificial spectra; they do not include the intrinsic scatter in CIV/HI. The dotted curve will be discussed in §6.2 and the dashed curve in §6.3.

From this analysis, we confirm the results of Rauch et al. (1997a) and HDHWK that a mean metallicity of $[\text{C}/\text{H}] \approx -2.5$ with a small amount of spatial scatter, together with an ionizing background of the HM shape, reproduces the observed distribution of CIV/HI ratios in Q1422 quite well. Note that the cosmological model and Ω_b value used for our simulations are substantially different from those used by HDHWK, demonstrating the overall lack of sensitivity of the mean metallicity determination to these assumptions. We now turn our attention to the question of whether this metallicity distribution is consistent with observations of OVI absorption.

5. Searching for OVI Absorption

5.1. Narrow Line Detection Algorithm

Coincident HI absorption complicates the detection of OVI(1032Å,1037Å) lines in quasar spectra. For Q1422, OVI is detectable only below about 4800Å, lying in a region with a high density of Ly α (1216Å) and Ly β (1026Å) absorbers.

OVI lines are expected to be narrower than HI lines because thermal broadening is a factor of four lower. However, as one goes to lower density structures, broadening by residual Hubble flow across the absorbing region becomes progressively more important (Weinberg et al. 1998), making OVI lines broader than naively predicted by thermal broadening. Nevertheless, we expect that the distribution of OVI line widths will have a tail to smaller b -parameter (i.e., Gaussian velocity width) than HI line widths. Since our goal is to distinguish OVI absorption from HI absorption rather than to identify all possible OVI features, we focus on this tail of narrow OVI lines in our detection algorithm.

Figure 5 shows a comparison between a roughly 100Å segment in one of our continuous artificial spectra versus the spectrum of Q1422. The top panel shows an artificial spectrum in the same wavelength range without any metals added (i.e., only Lyman series absorption). The second panel shows the absorption caused purely by OVI, including both doublet lines. The

third panel shows the artificial spectrum with a metallicity of $[C/H] = -2.5$ and $[O/C] = +0.5$, essentially corresponding to the optical depth sum of the first and second panels, since no other ions contribute significantly in this wavelength range. The bottom panel shows Q1422 between 4510Å and 4605Å. The noisy lines represent the data; the smooth curves will be explained below.

From the third panel of Figure 5 it is apparent that some narrow features from OVI do survive despite the blanketing by HI. We tried a variety of algorithms to quantify the presence of these additional narrow features. The standard technique of decomposing the full spectrum into a superposition of Voigt profiles (which are effectively just Gaussian optical depth profiles in this low column density regime) proved ineffective. Many of the HI features are intrinsically asymmetric, and in Voigt profile decomposition narrow components are often introduced to fit the wings of these asymmetric lines. It is therefore more useful to focus on *isolated* narrow lines.

As an alternative to Voigt profile decomposition, we developed a much simpler algorithm that searches for spectral features that dip by more than 4σ and then return to their original level all within a very small velocity interval, e.g. 18 km s^{-1} (4–5 pixels). The 4σ criterion eliminates noise spikes, while the velocity range criterion is tuned to optimally select out the tail of narrow OVI lines that we would like to identify. We call this procedure our *narrow line detection algorithm*. After identifying the narrow feature, we fit it using a Voigt profile to obtain its column density and b -parameter. The identification and fits are shown as the smooth curves in Figure 5. As can be seen there, this algorithm effectively picks out many of the narrow OVI features that survive HI blanketing.

Occasionally, narrow lines are detected in the spectrum even without any metals (top panel of Figure 5). These narrow lines arise primarily at velocity caustics, which produce HI lines whose widths are close to those expected from thermal broadening. Figure 5 shows, however, that these false detections are significantly fewer in number than the true OVI lines for an oxygen abundance of $[O/H] = -2.0$. Figure 5 suggests that narrow lines are seen much more rarely in Q1422 (bottom panel) than in an artificial spectrum with $Z = -2.5$. These qualitative impressions are borne out by the statistics we present in the next section.

5.2. Statistics of Narrow Lines

We apply the narrow line detection algorithm to Q1422 between 4025Å and 4745Å. We apply the same algorithm over the same interval to the six artificial Q1422 spectra, first with no metals, then with a series of uniform metallicity values ranging from $Z = -3.4$ to $Z = -2.2$. At each metallicity we count the number of narrow lines detected. For Q1422, we detect 11 narrow lines, while in the zero-metallicity case we detect an average of around seven per artificial spectrum. Figure 6 shows the number of narrow features detected in the artificial spectra as a function of metallicity, quantitatively confirming the inference from Figure 5 that a metallicity of $[C/H] = -2.5$ with a relative overabundance $[O/C] = +0.5$ is strongly inconsistent with the paucity of narrow

features in the spectrum of Q1422. At $Z = -2.5$, the expected number of narrow line detections is 63 ± 8 (where the 1σ error bars reflect the variance over the six artificial spectra), which is inconsistent with the Q1422 data at $\gtrsim 6\sigma$ level.

We can strengthen this conclusion with an improvement to our narrow line detection algorithm. The narrow lines we identify as candidate OVI lines should have a doublet companion if they are indeed OVI. While HI blanketing usually prevents actual identification of the doublet companion feature, one can at least require that there be enough absorption at the doublet position to obscure (or represent) the companion line. Since we do not know which member of the doublet to assign to any given narrow line, the stronger line at 1032\AA or the weaker line at 1037\AA , we must examine both doublet wavelength positions; if neither contains sufficient absorption, we can exclude that line from our list of OVI candidates.

We can apply a similar technique to associated HI absorption. From the LOX plot of Figure 2, one can see that OVI lines are not expected to be detectable for systems with $N_{\text{HI}} \lesssim 10^{13} \text{cm}^{-2}$. Below these densities, the amount of oxygen is small and much of it has been ionized to OVII. This N_{HI} cutoff is for $Z = -2.5$, and it scales with metallicity. Using this metallicity-dependent relation, we can examine the spectrum at the two relevant positions to see if there is sufficient absorption to allow a Ly α line of the appropriate HI column density. If not, we can exclude that line. The HI selection criterion removes more potential OVI detections than the doublet companion selection criterion.

Applying these two additional constraints, we obtain the results plotted in Figure 7. The number of candidate OVI lines in Q1422 has dropped from 11 to 5 at $Z = -2.5$. The number of lines excluded now depends on the assumed metallicity, even for Q1422, since the associated HI line strength required to exclude a narrow line as OVI depends on the metallicity. A slightly smaller number of lines (~ 4 on average) are excluded from the no-metallicity artificial spectra (when narrow lines are excluded by requiring $N_{\text{HI}} > 10^{13}$, as at $Z = -2.5$), making Q1422 compatible with having no narrow lines due to OVI. A slightly larger number of lines are excluded in the spectra with metals. At $Z = -2.5$, however, this larger number still represents a much smaller fraction of the total number of narrow lines detected; the number of expected OVI detections is now 54 ± 6 , inconsistent with Q1422 by $\gtrsim 8\sigma$. The number of narrow lines in the artificial spectra is consistent with that in Q1422 only for metallicities $Z \lesssim -3.2$.

In §6.1, §6.2, and §6.3 we examine the sensitivity of this result to the various assumptions we have made in our modeling. Before that, we examine some physical properties of the narrow lines identified by our algorithm.

5.3. HI Column Densities Associated With Narrow Lines

We first focus on the artificial spectra with $Z = -2.5$. Even though this model is inconsistent with the Q1422 data, it is helpful to examine the properties of its OVI absorbers and associated

HI and CIV lines in order to reinforce the points made earlier in §3.

From the LOX plot of Figure 2, we claimed that OVI should trace low column density (and hence low density) systems. In order to quantify this, we associate HI lines with each narrow feature in our artificial spectra. Since we cannot tell directly from an artificial spectrum whether a feature is the stronger or weaker OVI component, we sum the column densities of nearby HI lines within 25 km s^{-1} of the two appropriate wavelengths, then use the greater of the two column densities. Owing to the high density of HI lines with $N_{\text{HI}} \lesssim 10^{14} \text{ cm}^{-2}$, this is an inexact procedure, as it is difficult to associate a single HI feature with a given OVI line (even more so than in the case of CIV). Nevertheless, summing all the lines within 25 km s^{-1} (the typical width of HI features) provides a reasonable estimate of the HI column density. We also apply a similar procedure to CIV absorbers identified in our artificial spectra.

We plot the histogram of associated HI column densities for OVI (narrow) and CIV lines in Figure 8. OVI lines trace HI with column densities down to 10^{13} cm^{-2} (associated HI lines identified below this column density are probably spurious) with a maximum sensitivity for systems around 10^{14} cm^{-2} . CIV traces systems with HI column densities down to $10^{14.5} \text{ cm}^{-2}$, with a maximum sensitivity around 10^{15} cm^{-2} . Thus, as we stated earlier, OVI lines trace lower density regions, and the “typical” HI column density traced by OVI absorbers is around 10^{14} cm^{-2} . The gas density in $N_{\text{HI}} \approx 10^{14} \text{ cm}^{-2}$ systems is close to the mean cosmic baryon density. Also as we stated earlier, the majority of lines with detectable OVI absorption would have no detectable associated CIV absorption.

5.4. Column Densities and b -parameters of Narrow Lines

In Figure 9 we plot the b -parameter of OVI-selected narrow lines (i.e., those tallied in Figure 7) against the column density (inferred by assuming that they are HI lines). In the upper left panel we show all the narrow lines in the six artificial spectra with $Z = -2.5$. In the lower left panel we show the narrow lines identified in the artificial spectra with no metals. The lower right panel shows the “extra” metal lines, i.e. those in the $Z = -2.5$ spectra but not in the zero-metallicity artificial spectra. Finally, the upper right panel shows the OVI-selected narrow lines in Q1422.

This figure shows that our narrow line detection algorithm effectively picks out the tail of narrow lines that arise owing to the presence of OVI. The second panel of Figure 5 (the artificial spectrum with only OVI absorption) shows that many OVI features detectable by eye do not pass our narrow line selection criteria. Still more OVI features are subsumed by HI absorption. The OVI lines that we do identify tend to be both strong and narrow.

There are many more narrow OVI lines in the $Z = -2.5$ artificial spectra than seen in the no-metallicity spectra. If one further considers only lines with $b < 10 \text{ km s}^{-1}$ (dotted line in Figure 9), there are no lines in the zero metallicity case, while there are many such lines in the $Z = -2.5$ case. The simulation tests therefore imply that any narrow line detected by this

algorithm having $b < 10 \text{ km s}^{-1}$ has a good chance of being a true OVI line, if not an intervening metal line from a low redshift absorption system.

5.5. Individual Narrow Line Systems in Q1422

We now examine in detail the four narrow lines found in Q1422, shown in the upper right panel of Figure 9. There is a fifth narrow line, but it has $b \approx 25 \text{ km s}^{-1}$, and it appears to be due to a single cold pixel in Q1422, so we discard it. Two of the remaining lines have $b < 10 \text{ km s}^{-1}$, making them strong candidates for OVI, while one line (the circled point in Figure 9) is the OVI system identified by KT97. For each of these four systems, the doublet position is subsumed by an HI line, so no direct confirmation of OVI absorption is possible.

Figures 10(a-d) show the four narrow systems identified in Q1422, along with the associated Ly α , CIV1548, and CIV1551 spectral regions. For the various regions, the solid line corresponds to the assumption that the narrow feature is OVI1032, while the dashed line assumes OVI1037 absorption. The other ions have been offset in flux for ease of viewing.

The first system, at 4276.5\AA , has a b -parameter of only 5.4 km s^{-1} . If it is OVI1032, it has an associated Ly α line with $N_{\text{HI}} \approx 10^{14.5} \text{ cm}^{-2}$ (confirmed by the Ly β component, not shown), but no detectable CIV absorption (giving $N_{\text{CIV}} < 10^{11.5} \text{ cm}^{-2}$ at a 3σ level). Since it is a very weak line that is just above our 4σ detection threshold, there is a possibility that it is an abnormally large noise fluctuation. It would be interesting to confirm this feature using another spectrum of Q1422+231, e.g. KT97. If it is an OVI line, it has $N_{\text{OVI}} \approx 10^{13.2}$, and we can determine the metallicity and oxygen overabundance assuming an HM spectrum, the density-column density relation from equation (2), and the solar abundance values from Anders & Grevesse (1989). The ionization fractions are then 5.4% for CIV, 35% for OVI, and $10^{-4.9}$ for HI, giving $[\text{O}/\text{H}] = -2.5$ and $[\text{C}/\text{H}] \lesssim -2.9$. Thus this system, if OVI, would have a metallicity of $Z \lesssim -2.9$, with an overabundance of $[\text{O}/\text{C}] \gtrsim +0.4$. These values are quite consistent with the metallicity distribution inferred from the statistics of narrow lines.

The second system (4278.9\AA) has $b = 13.7 \text{ km s}^{-1}$. With only a modest Ly α line nearby (corresponding to this system being OVI1037), and no CIV absorption, it seems quite likely that this system is a narrow HI line.

The third system (4517.2\AA) is a deep, narrow line with $b = 7.5 \text{ km s}^{-1}$. However, there is a limited amount of corresponding Ly α absorption, and no CIV absorption. For such a large OVI line ($N_{\text{OVI}} \approx 10^{14} \text{ cm}^{-2}$), it is virtually inconceivable that there would be so little Ly α and no CIV absorption. This contradiction favors an alternative explanation: this is an intervening metal line from a low redshift absorption system.

The fourth and final system is the one presented in KT97 and discussed in §3. The associated CIV absorption provides compelling evidence that this is indeed an OVI line. We measure a

b -parameter of 13 km s^{-1} , as opposed to 10 km s^{-1} from KT97. Since we do not remove known Ly β absorption before fitting, the KT97 value is probably more accurate for the OVI feature itself.

All in all, of the four lines, only one is confirmed to be OVI (the KT97 system), with another having some likelihood of being OVI. This detailed analysis emphasizes the paucity of detectable OVI absorption in Q1422.

6. Varying the Theoretical Assumptions

6.1. Overabundance and Uniformity of Oxygen

Throughout this paper we have assumed an overabundance of $[\text{O}/\text{C}] = +0.5$ compared with solar abundance ratios. Had we assumed solar abundance ratios, we would have favored the opposite conclusion, that a uniform metallicity of $[\text{C}/\text{H}] = -2.5$ is (within uncertainties) consistent with the OVI data. This possibility therefore merits further discussion.

The theoretical motivation for oxygen overabundance is the assumption that early star formation produced enrichment patterns characteristic of Type II supernova yields, which have enhanced representation of α -process elements. High redshift enrichment almost certainly relies on Type II supernovae; in a blowout model, both energetic and time constraints require Type II supernovae (Miralda-Escudé & Rees 1998), while in a tidal stripping model (Gnedin & Ostriker 1997; Gnedin 1998), there is insufficient time to produce a large number of Type I supernovae. Direct evidence for Type II enrichment patterns in the early universe comes from local halo stars, which show an overabundance of oxygen relative to carbon of 3–5 (Edvardsson et al. 1993), and there is evidence that the very earliest stars are even more overabundant in α -process elements (McWilliam 1997). There is also mounting evidence for Type II enrichment patterns at high redshift in forming galaxies (Pettini et al. 1995) and in damped Ly α absorbers (Lu et al. 1996a). Thus an overabundance of $[\text{O}/\text{C}] \sim +0.5$ for the IGM at redshifts $z \gtrsim 3$ seems a reasonable, and perhaps even somewhat conservative, assumption.

We have also assumed a uniform metallicity. From the CIV data, one sees that at least some spatial scatter in metallicity is likely. Such a scatter applied to the simulations would serve to *strengthen* our conclusions, because it would tend to increase the number of OVI systems in the strong-absorption tail of the distribution, and these stronger lines are more likely to be detected despite coincident HI absorption. For spatial variations in the ionizing background, the situation is more complex, but a similar argument is still probably valid as long as there is no systematic softening of the ionizing background above 114 eV.

6.2. Reionization Heating

Our simulation assumed ionization equilibrium (balance between recombination and ionization rates) at all times when computing ionic abundances. Departures from equilibrium abundances can, under some circumstances, allow substantial heating of the IGM during the reionization epoch (Miralda-Escudé & Rees 1994). The low density gas that produces the Ly α forest loses energy mainly from adiabatic expansion, so the cooling timescale is comparable to the Hubble time. The relation between gas temperature and density in the IGM therefore depends on the assumed reionization epoch and associated heat injection (Hui & Gnedin 1997). Our equilibrium abundance approach yields the temperature-density relation that arises for minimal heating or a high reionization redshift. The higher temperatures that arise in plausible alternative reionization scenarios could in principle have a significant effect on our OVI modeling because the ionization fractions are sensitive to temperature.

One example of the effect of different reionization assumptions appears in figure 7 of Rauch et al. (1997b), which shows the difference in the density-temperature relation between a simulation run assuming ionization equilibrium (Katz, Weinberg & Hernquist 1996) and a simulation in which reionization occurred at $z \gtrsim 6$ and the heat input was tracked in a non-equilibrium manner (Miralda-Escudé et al. 1996). The latter simulation shows hotter temperatures in the low-density regions, with the discrepancy growing towards lower densities, as expected.

While we are currently unable to perform non-equilibrium simulations of reionization, we can add the difference in the temperatures *post facto* to estimate the potential effect of the additional thermal energy. Thermal pressure gradients are small compared to gravitational forces in low density regions, so the dynamics of the gas should be unaffected by higher temperatures, and the *post facto* change of the temperature-density relation therefore accounts accurately for the full effect of reionization heating. In support of this claim, we note that the distributions of the gas density for the two simulations considered by Rauch et al. (1997b) are very similar (see their figure 6).

The difference in temperatures in the two Rauch et al. (1997b) simulations can be approximated as

$$T_{\text{hot}} = T_{\text{equil}} 2^{[1 - \log(\rho/\bar{\rho})]} \quad \text{for } \rho/\bar{\rho} < 10, \quad (4)$$

where ρ is the density and $\bar{\rho}$ is the mean baryonic density. There is no difference for overdensities greater than ten, as the cooling time there is sufficiently short to equilibrate the system. By adding this heat to each particle of our simulation before we construct our artificial spectra, we obtain a set of “reionization heated” spectra. For these spectra, the factor by which the HM photoionizing background spectrum must be multiplied in order to match the mean transmission of Q1422 is 0.86 ± 0.13 .

We perform the same CIV analysis on the reionization heated spectra to determine the mean metallicity that should be inferred from the observed CIV abundance in this hotter IGM model.

We find that reionization heating has a negligible effect (see the dotted line in Figure 4) because most of the CIV absorption arises from systems with overdensities greater than ten, translating to a column density $N_{\text{HI}} \gtrsim 10^{14.7} \text{cm}^{-2}$ (cf. eqn. [2]; also see Figure 8).

For our OVI analysis, the results are somewhat more sensitive to reionization heating because OVI arises in lower density regions. If the IGM is hotter, more oxygen is ionized to OVII. However, this is countered by the fact that to match the mean transmission of Q1422 in the Ly α forest region, a hotter IGM requires a lower ionizing background intensity. A hotter IGM also means that the tail of OVI lines below a given b -parameter is smaller, reducing the efficiency of our narrow line search procedure for detecting OVI and therefore increasing the OVI abundance inferred from a given number of detections. This last effect turns out to be minimal; the dominant effects are the first two, with the first being somewhat more important. The results are shown in Figure 11 (solid line), indicating that the maximum metallicity allowed for agreement with the OVI data is around $Z = -3.0$ instead of $Z = -3.2$. So, in the final analysis, the effect of reionization heating does not significantly change our overall conclusion that a uniform metallicity of $Z = -2.5$ is inconsistent with the OVI data.

6.3. Ionizing Background Spectrum

A more dramatic effect arises if the ionizing background contains many fewer photons capable of ionizing oxygen to OVI. Such a scenario might arise if, for example, helium reionization has not occurred by $z \sim 3$. We consider an idealized model of such a scenario in this section.

To test the sensitivity of our analysis to the softness of the assumed ionizing background, we generate a new J_ν with the shape from HM, except that the intensity is reduced by a factor of ten above 4 Ry; we refer to this as the *cut* J_ν . We generate a new set of artificial spectra using this cut J_ν ; the mean transmission is virtually identical to that of the original spectra because these high energy photons do not significantly affect the HI opacity. With the cut J_ν , CIV is much more common, and we find the mean metallicity for agreement with CIV data to be $[\text{C}/\text{H}] \approx -3.3$, as shown by the dashed line in Figure 4. When we apply the same narrow line detection procedure to spectra generated with the cut J_ν , we obtain the results presented in Figure 12. This shows that a metallicity of $Z < -2.9$ is in agreement with the OVI data. The cut J_ν scenario therefore implies a mean metallicity in the Ly α forest of around $Z \approx -3.3$. With the assumed $[\text{O}/\text{C}] = +0.5$, this scenario is consistent with a uniform metallicity; however, we shall show in §7 that a cut J_ν also requires a much higher oxygen overabundance, thus a metallicity gradient is still required.

There is some evidence that helium reionization occurs around $z \approx 3$, from a sudden drop in the SiIV/CIV ratio near that redshift (SC96; S98). This evidence is controversial, as other studies have not detected such a drop (Boksenberg 1998), though S98 shows that it appears with several different methods of analysis. If many more OVI lines were detected in quasar spectra at $z \lesssim 3$, this would provide an interesting argument in favor of the helium reionization scenario. While

Q1422 is poorly suited for this investigation, we hope that in the future we can examine other quasar spectra over a wider range of redshifts. Figure 4 implies that an increase in OVI due to a change in the ionizing background shape should be accompanied by an increase in CIV/HI ratios.

One piece of evidence arguing that helium *has* been reionized by this epoch is the measurement of the HeII opacity at $z \approx 3.3$ by Hogan, Anderson & Rugers (1997). From the strength of a HeII discontinuity about 5.3\AA from quasar Q0302-003, they find $\bar{\tau}_{\text{HeII}} \approx 2_{-0.5}^{+1}$ (2σ errors). The HM spectrum we use yields $\bar{\tau}_{\text{HeII}} \approx 2.6$ at $z = 3$, while the cut J_ν spectrum yields $\bar{\tau}_{\text{HeII}} \approx 6.3$, well outside the quoted uncertainty of the observed optical depth. However, the observation of patchy HeII absorption at $z \sim 3$ by Reimers et al. (1997) suggests that HeII reionization does occur near this redshift, and that the Hogan, Anderson & Rugers (1997) measurement in the immediate vicinity of Q0302 might provide a poor estimate of the overall mean HeII absorption. A more secure determination of $\bar{\tau}_{\text{HeII}}$ at $z \gtrsim 3$ may have to await the deployment of the Cosmic Origins Spectrograph on the Hubble Space Telescope.

7. Detection of OVI by the Optical Depth Ratio Technique

7.1. Algorithm and Q1422 Results

Our narrow line detection results are consistent with either the metallicity being lower in lower density regions or the ionizing background being significantly truncated above 4 Ry (assuming a reasonable overabundance of oxygen relative to carbon). In order to distinguish between these two scenarios, we apply a different algorithm for detecting OVI that was developed by S98. In this algorithm, no metal line identification is done; rather, the presence of metals is assessed statistically by a pixel-by-pixel search for excess optical depth at the expected position of associated absorption. In this section we describe this *optical depth ratio* technique.

Using this technique, we search for OVI absorption associated with all regions of space showing significant CIV absorption. For all pixels redwards of the quasar’s Ly α emission peak, we first identify pixels that have $\tau > 0.05$. From these we select pixels consistent with absorption arising from the weak doublet component of CIV (1551\AA). Specifically, we only accept a pixel if the optical depth at the strong doublet component’s position (1548\AA) is at least double the optical depth at the weak component’s position (with some allowance for noise). The final subset of pixels represents all regions along the line of sight to the quasar showing significant CIV absorption. For Q1422, 376 out of a total of roughly 25,000 pixels redwards of the Ly α emission peak are selected as having significant CIV absorption. For each of the selected pixels, we find the optical depth at the associated OVI position and calculate the “apparent column density ratio”:

$$\frac{N_{\text{OVI,app}}}{N_{\text{CIV}}} = \left(\frac{\tau_{\text{OVI}}}{\tau_{\text{CIV}}} \right) \left(\frac{\lambda_{\text{CIV}} f_{\text{CIV}}}{\lambda_{\text{OVI}} f_{\text{OVI}}} \right), \quad (5)$$

where τ is the optical depth, λ is the rest wavelength, and f is the oscillator strength for each

ion. $N_{\text{OVI,app}}$ is not the true OVI column density because there is a significant contribution from coincident HI absorption.

Although the LOX plot of Figure 2 shows that the detectability of CIV and OVI peaks at different HI column densities, it also shows that the weaker (and therefore more common) CIV lines, associated with $N_{\text{HI}} \sim 10^{15} \text{cm}^{-2}$, should have significant amounts of photoionized OVI. This is seen when we apply the optical depth ratio technique to artificial spectra with oxygen ($[\text{O}/\text{H}] = -2.0$) and without oxygen, the latter being used to assess the contribution from coincident HI absorption. The results are shown in Figure 13, as a histogram of $N_{\text{OVI,app}}/N_{\text{CIV}}$ (this is similar to Figures 20e-g from S98, except that S98 uses randomly selected regions of the observed spectrum instead of a zero-metallicity model spectrum as the “control” sample). There is a significant excess of OVI seen in the $[\text{O}/\text{H}] = -2.0$ spectra (solid line) as compared to the spectra without no oxygen (dotted line); this is mostly due to photoionized OVI associated with CIV absorbers, as the covering fraction of collisionally ionized OVI is quite small. We also apply the technique to Q1422, and find a significant presence of OVI, consistent with S98. The Q1422 results (dashed histogram in Figure 13) are seen to be in better agreement with the $Z = -2.5$ spectra than with the zero-metallicity spectra. We will quantify these results further in the next section.

Our conclusion from optical depth ratios that $[\text{O}/\text{H}] \approx -2.0$ may seem inconsistent with our earlier conclusion from narrow lines that $[\text{O}/\text{H}] \leq -2.5$, but it is not, *provided* that the IGM metallicity is lower at lower gas densities. With the narrow line detection algorithm, we are examining *all* regions of space for OVI absorption, so the measure is weighted towards the low-density regions that occupy most of the volume. Conversely, the optical depth ratio technique examines regions of space selected to have significant CIV absorption, which are typically higher density regions. In fact, from §4 we *know* the metallicity in these regions is $Z \approx -2.5$ in the full HM spectrum case, or $Z \approx -3.3$ in the case of our cut J_ν spectrum (cf. §6.3). Thus, we can use the detection of OVI in these regions as a probe of the shape of the ionizing background and the assumed oxygen overabundance, as we will show in the next section.

For regions that have detectable CIV absorption, the optical depth ratio technique is significantly more sensitive to the presence of OVI than the narrow line detection algorithm. Because most OVI positions are contaminated by HI absorption, the opportunity to detect a narrow OVI line associated with CIV is very rare. The optical depth ratio technique can still achieve a statistical detection of OVI in such cases because it examines only the precise locations of expected OVI absorption and compares their mean optical depth to an OVI-free control sample.

We attempted to quantify the presence of OVI associated with Ly α absorption of a given optical depth, but were unsuccessful. The optical depth ratio technique is much less reliable when used with HI rather than CIV, since the typical line widths of HI features are significantly different from those of CIV or OVI; it is only because OVI and CIV have similar thermal broadening (and identical bulk flow broadening because we are examining the same physical region) that optical

depths at associated wavelengths can be meaningfully compared.

7.2. Constraining Ionization Conditions and Metallicity Gradient

We now apply the optical depth ratio technique to artificial spectra with varying metallicity. For the artificial spectra, the assumed $[C/H]$ is held fixed at the value that produces agreement with the CIV data (i.e. -2.5 for the HM spectrum and -3.3 for the cut spectrum), and we vary only $[O/H]$ (or equivalently, the oxygen overabundance). We plot the median value of $N_{\text{OVI,app}}/N_{\text{CIV}}$, since the median provides the most robust characteristic quantity in this highly skewed distribution. The median $N_{\text{OVI,app}}/N_{\text{CIV}} \approx 8.3$ for Q1422, and ≈ 2.6 for the artificial spectra without oxygen. These values are shown as the horizontal dashed and dotted lines in Figure 14, respectively. The varying $[O/H]$ case is shown by the solid line, with the error bars as usual computed over the six artificial spectra (the error bars on the other artificial spectra measurements are comparable). Agreement with Q1422 is seen to occur at $[O/H] \approx -2.0$, and given that the metallicity of these regions is $[C/H] \approx -2.5$, this implies $[O/C] \approx +0.5$. Thus for the case of the HM spectrum, we have independently determined that our assumed oxygen overabundance is consistent with Q1422.

We now examine the cut J_ν spectrum case, as shown by the dot-dashed line in Figure 14. With a softer spectrum, OVI is much less abundant and CIV is more abundant, meaning that a significantly higher overabundance of oxygen is required to reach agreement with the Q1422 data for OVI associated with CIV regions. Agreement is reached with Q1422’s median $N_{\text{OVI,app}}/N_{\text{CIV}}$ for $[O/H] \approx -1.0$, which when combined with $[C/H] \approx -3.3$ for the cut spectrum implies $[O/C] \approx +2.3$. A factor of $\gtrsim 100$ oxygen overabundance seems fairly implausible, as no set of objects has ever been observed to have α -process overabundances approaching this level.

We conclude that the regions showing CIV absorption are in much better agreement with a HM spectrum with no softening above 4 Ry, and therefore that most helium is doubly ionized by redshift $z \sim 3.6$. This scenario is also consistent with an oxygen overabundance of $[O/C] \approx +0.5$.

free We can assess the presence of a gradient of metallicity with density, free from assumptions about the oxygen overabundance, by comparing $[O/H]$ from the narrow associated with CIV regions with the limits on $[O/H]$ in lower density gas from the narrow line detection algorithm. For the HM spectrum case, CIV regions have $[O/H] \approx -2.0$, while the narrow line search $[O/H] \lesssim -2.5$, implying at least a factor of 3 decrease in metallicity at lower densities. For the cut J_ν spectrum, CIV regions have $[O/H] \approx -1.0$, whereas the narrow line search yields $[O/H] \lesssim -2.9$, implying an even *greater* metallicity gradient. Thus regardless of the assumed ionizing background, a metallicity gradient is required to match the observed amount of OVI from both detection methods, barring the unlikely scenarios that the metagalactic ionizing flux is significantly *harder* than the HM spectrum, or the oxygen overabundance is significantly lower in the lower density regions.

7.3. IGM with Patchy Ionization Conditions

As mentioned before, S98 detected a significant jump in SiIV/CIV ratio above $z \approx 3$, that when combined with the SiIV/CIV ratio above $z \approx 3$, which, when combined with photoionization models, is consistent with an ionizing spectrum heavily truncated (by a factor $\gtrsim 100$) above 4 Ry. This inference is in direct contradiction with the results of the previous section. One way to reconcile these results may be to invoke an IGM that has a patchy ionization structure. This type of structure is implied by the HeII measurements of Reimers et al. (1997), as stated in §6.3, and has been suggested by S98 to explain the significant presence of OVI detected at $z \gtrsim 3$. In this section we consider a simplistic, “50/50” model of such a patchy IGM to determine the implications for our OVI detections.

Consider a universe where half the volume has already reionized helium (and hence has an HM spectrum), and half the volume has a significantly truncated ionizing flux above 4 Ry (as in our cut J_ν spectrum). CIV absorption then implies a mean metallicity of $[C/H] \approx -2.9$. This value can be determined from Figure 4, as this is the metallicity where the solid (HM spectrum) and dashed (cut spectrum) curves are roughly equally above and below the observed $\langle \log(N_{CIV}) \rangle$ of Q1422. The additional scatter introduced by the varying ionization conditions implies that there can be virtually no intrinsic spatial scatter in the metallicity of CIV absorbers. Similarly, bisecting the solid and dot-dashed curves in Figure 14 implies agreement with the Q1422 optical depth ratio results at $[O/H] \approx -1.7$. Taken together, the $[C/H]$ and $[O/H]$ constraints imply $[O/C] \approx +1.2$ in the 50/50 model. This overabundance is perhaps marginally plausible if one invokes enrichment almost entirely from high-mass stars yielding a high fraction of α -process elements.

The narrow line detection results become statistically consistent with the Q1422 data only for $[O/H] \lesssim -2.5$ (metallicity $Z \lesssim -3$), as seen by bisecting the solid and dot-dashed curves in Figure 12. Thus, a metallicity gradient is still required in the 50/50 model, as the optical depth ratio technique (tracing CIV regions only) yields $[O/H]$ higher by $\approx +0.8$ dex than the narrow line detection technique (tracing mostly lower density regions).

While the 50/50 patchy IGM model is marginally consistent with the OVI data, it remains to be seen whether such a scenario is consistent with the observations of SiIV/CIV by S98. Currently, with only one quasar spectrum available to us, we do not have sufficient statistics to investigate SiIV in detail; we plan to conduct these investigations when more data become available, preferably at $z \lesssim 3$ as well as at $z \gtrsim 3$.

8. Discussion and Conclusions

We present a systematic search for OVI absorption in the spectrum of Q1422+231 ($z = 3.62$), using a narrow line detection algorithm proven effective at identifying OVI absorption in artificial spectra, and an optical depth ratio technique introduced by S98. The first technique traces OVI

predominantly in systems with $10^{13.5} \lesssim N_{\text{HI}} \lesssim 10^{15} \text{cm}^{-2}$, whereas the second technique traces only OVI associated with CIV absorption, i.e. in $10^{14.5} \lesssim N_{\text{HI}} \lesssim 10^{16} \text{cm}^{-2}$ systems. By comparing Q1422 and artificial spectra having varying metallicities, we determine that

1. [O/H] must be lower in lower density regions, for either an HM ionizing background or an ionizing background significantly truncated above 4 Ry. If [O/C] is constant in systems up to $N_{\text{HI}} \sim 10^{16} \text{cm}^{-2}$, our results imply that regions traced by $N_{\text{HI}} \lesssim 10^{14} \text{cm}^{-2}$ systems (corresponding to gas at roughly the mean baryonic density) have a mean metallicity lower by at least a factor of 3 compared to regions traced by $N_{\text{HI}} \sim 10^{15} \text{cm}^{-2}$ systems (corresponding to a baryonic overdensity of ~ 10).
2. More than half the universe must have helium reionized by $z \sim 3$. If helium has completely reionized by $z \sim 3.6$ (the highest redshift probed by the Q1422 data), then our analysis implies $[\text{O}/\text{C}] \approx +0.5$, in good agreement with overabundance measurements of Type II supernovae enriched systems. If a significant portion of the universe has not reionized helium by $z \sim 3$ and therefore has a softer ionizing background spectrum, then the required oxygen overabundance is higher. For example, if half of the volume has not reionized helium, then $[\text{O}/\text{C}] \approx +1.2$, already greater than the observed overabundance of any class of Type II supernovae enriched systems. If the spectrum were soft throughout the universe at $z \gtrsim 3$ then an implausibly high overabundance, $[\text{O}/\text{C}] \approx +2.3$, would be required.

These conclusions are in good agreement with the recent study of Lu et al. (1998), who used composite spectra to investigate CIV absorption in systems with $10^{13.5} < N_{\text{HI}} < 10^{14} \text{cm}^{-2}$ and found that the metallicity of these absorbers must be $[\text{C}/\text{H}] \lesssim -3.5$. Cosmological simulations show that $N_{\text{HI}} \sim 10^{14} \text{cm}^{-2}$ roughly corresponds to the dividing line between overdense and underdense regions of the universe (though the value of N_{HI} that marks this division depends on redshift and, to a lesser extent, on cosmological parameters). Our results therefore imply that mildly overdense regions such as filaments and sheets have been enriched, while underdense regions are virtually chemically pristine. Simulations that self-consistently enrich the IGM by tracking metal production and transport find that a strong metallicity gradient is predicted between the mildly overdense and underdense regions (see figure 3 in Gnedin 1998); this predicted gradient is in good agreement with the Lu et al. (1998) data and with the scenario we present above.

Recent measurements of a jump in the SiIV/CIV ratio around $z \sim 3$ (S98) may be difficult to reconcile with conclusion (2) above. While we have yet to conduct a systematic comparison of SiIV in observed and artificial spectra, primarily because of the small numbers of SiIV systems detectable in our one available quasar spectrum, we expect our results will be in agreement with S98, who argues that such a jump requires a much softer ionizing background at $z \gtrsim 3$. One way to reconcile these results may be to invoke patchy helium reionization at that epoch, as suggested by Reimers et al. (1997); such a model may be tested in greater detail by searching for an anti-correlation between OVI and SiIV detections.

If helium reionization occurs around $z \sim 3$, our narrow line algorithm should yield many more OVI detections at redshifts $z \lesssim 3$. Such searches are difficult because of the poor blue sensitivity of the HIRES spectrograph (and complete loss of sensitivity at $\lambda \lesssim 3800\text{\AA}$), but quasar spectra do exist that could provide constraints down to $z \sim 2.7$. The presence of a substantial number of OVI lines in this regime would strongly favor the late helium reionization scenario; there is already some weak evidence that OVI is more abundant at $z \lesssim 3$ (S98). If OVI features continue to be virtually undetectable down to $z \sim 2.7$, this would be compelling evidence against the late helium reionization scenario, since the HeII absorption measurements of Davidsen, Kriss, & Zheng (1996) imply that helium has been reionized by this redshift. We hope to work with observers to attempt this search in the near future.

In a broader context, our work illustrates the power of combining cosmological hydrodynamic simulations of structure formation with high-quality quasar spectra to infer the ionization state and the enrichment history of the high-redshift IGM. Future observations and simulations promise a wealth of information, which, when combined, will help us to better understand the evolution of the IGM and its connection to early star formation and the epoch of primeval galaxies.

We are very grateful to Antoinette Songaila and Len Cowie for making their Keck quasar spectrum of Q1422+231 available to us. We thank Eric Linder and Antoinette Songaila for helpful discussions. We also thank Francesco Haardt and Piero Madau for providing us with their latest ionizing background in electronic form. UH acknowledges support from a postdoctoral research grant from the Danish Natural Sciences Research Council. This work was supported in part by the PSC, NCSA and SDSC supercomputing centers, by NASA theory grants NAGW-2422, NAGW-2523, NAG5-2882, NAG5-3111, and NAG5-3820, by NASA LTSA grant NAG5-3525, by NASA HPC/ESS grant NAG 5-2213, and by the NSF under grants AT90-18256 and ASC 93-18185. Finally, we acknowledge the essential contribution of S. Vogt and the HIRES team in building the instrument that made this kind of investigation possible.

REFERENCES

- Anders, E. & Grevesse, N. 1989, *Geochim. Cosmochim. Acta*, 53, 197
- Boksenberg, A. 1998, to appear in *Structure and Evolution of the IGM from QSO Absorption Line Systems*, Proc. 13th IAP Colloquium, eds. P. Petitjean and S. Charlot, *Nouvelles Frontieres*, Paris, astro-ph/9710258
- Burles, S. & Tytler, D. 1996, *ApJ*, 460, 584
- Burles, S. & Tytler, D. 1998a, *ApJ*, in press, astro-ph/9712108
- Burles, S. & Tytler, D. 1998b, *ApJ*, submitted, astro-ph/9712109
- Cen, R., Miralda-Escudé, J., Ostriker, J.P., & Rauch M. 1994, *ApJ*, 427, L9
- Cowie, L. L., Songaila, A., Kim, T.-S. & Hu, E. M. 1995, *AJ*, 109, 1522 Fontana, A.,
- Cowie, L. L., & Songaila, A. 1998, *Nature*, submitted
- Davé, R. 1998, to appear in *Structure and Evolution of the IGM from QSO Absorption Line Systems*, Proc. 13th IAP Colloquium, eds. P. Petitjean and S. Charlot, *Nouvelles Frontieres*, Paris
- Davé, R., Hernquist, L., Weinberg, D.H. & Katz, N. 1997, *ApJ*, 477, 21
- Davé, R., Dubinski, J. & Hernquist, L. 1997, *NewAst*, 2, 277
- Davidson, A. F., Kriss, G. A., & Zheng, W. 1996, *Nature*, 380, 47
- Edvardsson, B., Andersen, J., Gustafsson, B., Lambert, D. L., Nissen, P. E. & Tomkin, J. 1993, *A&A*, 275, 101
- Ferland, G.J. 1996, Univ. of Kentucky, Dept. of Astronomy, Internal Report
- Gnedin, N. Y. & Ostriker, J. P. 1997, *ApJ*, 486, 581
- Gnedin, N. Y. 1998, *MNRAS*, accepted, astro-ph/9709224
- Haardt, F. & Madau, P. 1996, *ApJ*, 461, 20 (HM)
- Haehnelt, M. G., Steinmetz, M. & Rauch M. 1996, *ApJ*, 465, L65
- Haiman, Z. & Loeb, A. 1997, *ApJ*, 483, 21
- Hellsten, U., Davé, R., Hernquist, L., Weinberg, D.H. & Katz, N. 1997, *ApJ*, 487, 482 (HDHWK)
- Hellsten, U., Hernquist, L., Katz, N. & Weinberg, D.H. 1998, *ApJ*, in press, astro-ph/9708090 (HHKW)

- Hernquist, L. & Katz, N. 1989, ApJS, 70, 419
- Hernquist, L., Katz, N., Weinberg, D.H., & Miralda-Escudé, J. 1996, ApJ, 457, L51
- Hogan, C. J., Anderson, S. F. & Rugers, M. H. 1997, AJ, 113, 1495
- Hu, E.M., Kim, T.S., Cowie, L.L., Songaila, A., & Rauch, M. 1995 AJ, 110, 1526
- Hui, L., & Gnedin, N. 1997, MNRAS, 292, 27
- Hu, W., & Sugiyama, N. 1996, ApJ, 471, 542
- Katz, N. & Quinn, T. 1995, TIPSYS manual
- Katz, N., Weinberg D.H., & Hernquist, L. 1996, ApJS, 105, 19
- Kim, T.S., Hu, E.M., Cowie, L.L., & Songaila, A. 1997 AJ, accepted, astro-ph/9704184
- Kirkman, D. & Tytler, D. 1997, ApJ, 489, L123 (KT97)
- Kirkman, D. & Tytler, D. 1998, ApJ, accepted, astro-ph/9701209
- Lu, L. 1991, ApJ, 379, 99
- Lu, L., Sargent, W. L. W., Barlow, T. A., Churchill, C. W., & Vogt, S. S. 1996a, ApJS, 107, 475
- Lu, L., Sargent, W. L. W., Womble, D. S., & Takada-Hidai, M. 1996b, ApJ, 472, 509
- Lu, L., Sargent, W.L.W., Barlow, T.A., & Rauch, M. 1998, ApJ, submitted, astro-ph/9802189
- Lynds, R. 1971, ApJ, 164, L73
- McWilliam, A. 1997, ARA&A, 35, 503
- Miralda-Escudé J., & Rees, M. J. 1994, MNRAS, 266, 343
- Miralda-Escudé, J., Cen, R., Ostriker, J.P., & Rauch, M. 1996, ApJ, 471, 582
- Miralda-Escudé, J. & Rees, M. 1997, ApJ, 478, L57
- Pettini, M., Lipman, K. & Hunstead, R. W. 1995, ApJ, 451, 100
- Rauch, M., Haehnelt, M. G., & Steinmetz, M. 1997a, ApJ, 481, 601
- Rauch, M., Miralda-Escudé, J., Sargent, W.L.W., Barlow, T.A., Hernquist, L., Weinberg D.H., Katz, N., Cen, R., Ostriker, J.P. 1997b, ApJ, 489, 7
- Reimers, D., Köhler, S., Wisotzki, L., Groote, D., Rodriguez-Pascual, P. & Wamsteker, W. 1997, A&A, 327, 890

- Sargent, W.L.W., Young, P.J., Boksenberg, A. & Tytler, D. 1980, *ApJS*, 42, 41
- Songaila, A. & Cowie, L. L. 1996, *AJ*, 112, 335 (SC96)
- Songaila, A. 1998, *AJ*, accepted, *astro-ph/9803010* (S98)
- Tytler, D., Fan, X.M., Burles, S., Cotrell, L., Davis, C., Kirkman, D. & Zuo, L. 1995, in *QSO Absorption Lines*, ed. G. Meylan (Springer-Verlag), 289
- Vogt, S. S., et al. 1994, *SPIE*, 2198, 326
- Weinberg, D. H., Hernquist, L., & Katz, N. 1996, *ApJ*, 477, 8
- Weinberg, D. H., Miralda-Escudé, J., Hernquist, L. & Katz, N. 1997, *ApJ*, 490, 564
- Weinberg, D.H., Hernquist, L., Katz, N., Croft, R. & Miralda-Escude, J. 1998, in *Proc. of the 13th IAP Colloquium, Structure and Evolution of the IGM from QSO Absorption Line Systems*, eds. P. Petitjean & S. Charlot, (Paris: Nouvelles Frontières), *astro-ph/9709303*
- Zhang, Y., Anninos, P. & Norman, M.L. 1995, *ApJ*, 453, L57

Fig. 1.— *Top left panel:* Q1422, with continuum fit and 4σ noise level shown for the Ly α forest region. *Bottom left panel:* One of the six continuous artificial spectra, with continuum fit and 4σ noise level shown. *Top right panel:* Ly α forest region of Q1422 after continuum normalization, with 4σ noise level. *Bottom right panel:* Normalized Ly α forest region of the artificial spectrum, with 4σ noise level.

Fig. 2.— Line Observability Index (LOX; see HHKW) for OVI and CIV, with $[C/H] = -2.5$ and $[O/C] = +0.5$. Solid curves are obtained by using the HM spectrum; dashed curves use the “cut” spectrum described in §6.3. The horizontal dotted line represents (roughly) the detectability limit redwards of the quasar Ly α peak, while the horizontal dot-dashed line represents the detectability bluewards. Note the increase in CIV detectability and decrease in OVI detectability using the cut spectrum.

Fig. 3.— CIV/HI ratios for all lines with $N_{\text{HI}} > 2 \times 10^{14} \text{cm}^{-2}$, in Q1422 (solid squares) and six continuous artificial spectra (open circles). The identical CIV identification and Voigt profile fitting routine has been applied to both data sets.

Fig. 4.— The variation of $\langle \log N_{\text{CIV}} \rangle$ with metallicity for the artificial spectra, as compared with the value obtained for Q1422 (horizontal line). For the spectra using the HM background, the agreement is achieved for $Z \sim -2.5$. The result is virtually unchanged by adding heat due to reionization (see §6.2), but is dramatically different ($Z \sim -3.3$) using the “cut” spectrum described in §6.3.

Fig. 5.— 4510Å to 4605Å segment from Q1422 and from one of the artificial spectra. Narrow lines have been identified and fitted (shown as smooth curves) according to the prescription described in §5.1. *Top panel:* Zero metallicity. *Second panel:* Only OVI absorption, with $[O/H] = -2$ (both doublet components). *Third panel:* Artificial spectrum with $Z = -2.5$. *Bottom panel:* Q1422. Note the observability of narrow lines in the artificial spectrum, as compared with Q1422.

Fig. 6.— The number of narrow lines detected in the artificial spectra with varying metallicity, versus the value for Q1422 (11 lines) and the artificial spectra without metals (7 lines). Agreement with Q1422 is reached only for metallicities around $Z \approx -3.0$.

Fig. 7.— The number of narrow lines selected for OVI compatibility using the doublet and HI criteria described in §5.2. At $Z = -2.5$, Q1422 has five possible OVI lines, while the no-metallicity artificial spectra have on average four. Consistency with Q1422 is reached only for metallicities $Z \lesssim -3.2$. This metallicity implicitly assumes an overabundance of oxygen $[O/C] = +0.5$, as expected for Type II supernovae-enriched gas.

Fig. 8.— Histogram of column densities of associated HI lines for OVI (narrow) lines and CIV lines, from the artificial spectra with $Z = -2.5$. The OVI lines trace lower density gas, with a peak sensitivity around $N_{\text{HI}} \approx 10^{14} \text{cm}^{-2}$, while CIV lines have a peak sensitivity around $N_{\text{HI}} \approx 10^{15.5} \text{cm}^{-2}$. In this scenario, most OVI lines detected will have no associated CIV absorption.

Fig. 9.— Scatter plot of b -parameters vs. column densities (fit assuming narrow line is HI) for the narrow lines identified in the six $Z = -2.5$ artificial spectra and selected for OVI, as compared with Q1422. *Upper left:* All narrow lines. *Lower left:* Narrow lines in zero-metallicity spectra. *Lower right:* Extra narrow lines due to the presence of OVI. *Upper right:* Narrow lines in Q1422. Note that no narrow lines with $b < 10 \text{ km s}^{-1}$ appear in the spectra without metals.

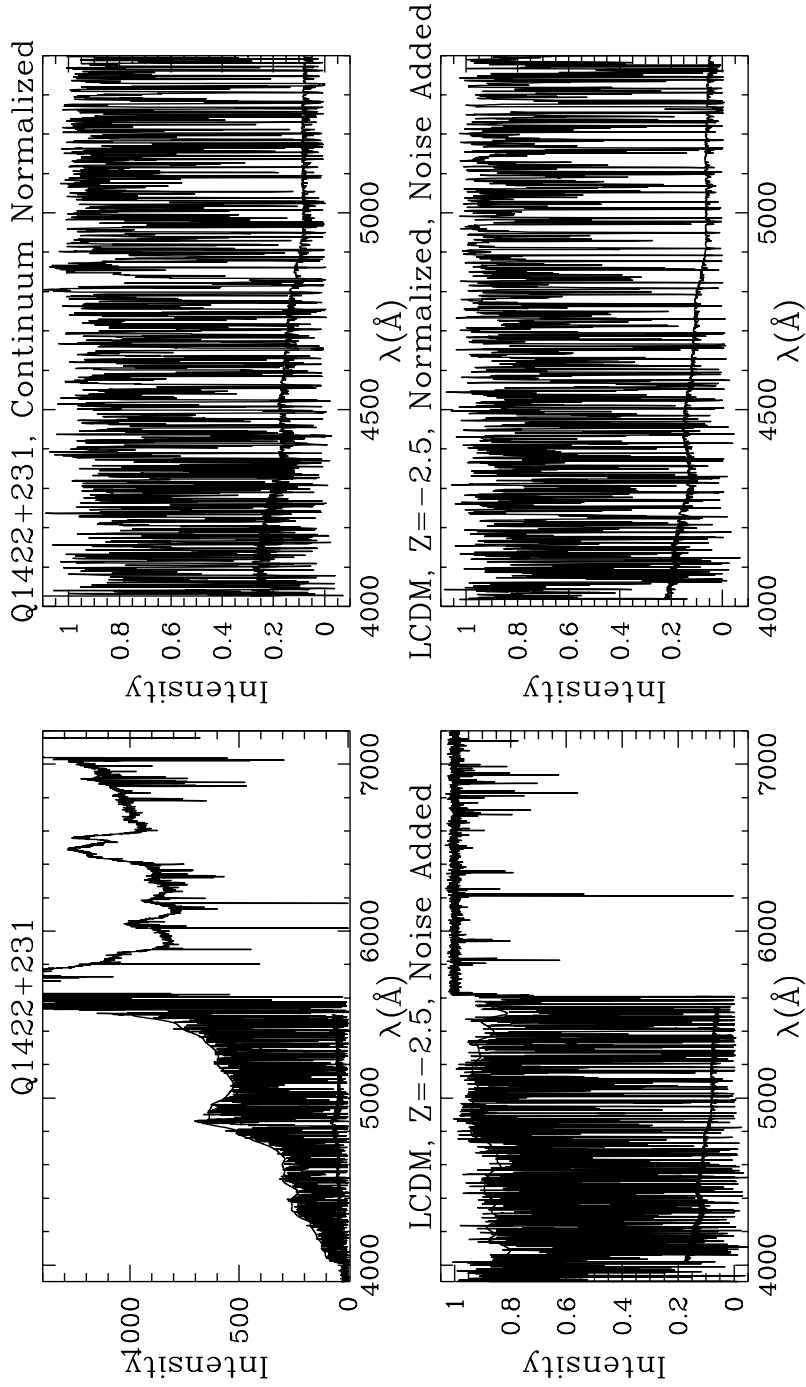
Fig. 10.— (a–d) Four individual candidate OVI systems in Q1422, with associated Ly α and CIV(1548Å,1551Å) regions. The solid line shows the region if the narrow line is OVI(1032Å), while the dashed line corresponds to assuming the narrow line is OVI(1037Å).

Fig. 11.— The number of narrow lines selected for OVI in artificial spectra with reionization heat added as described in §6.2. Agreement with Q1422 occurs at slightly higher metallicity, $Z \lesssim -3$. This is still inconsistent with a uniform metallicity of $Z = -2.5$ (assuming an overabundance of oxygen [O/C] = +0.5).

Fig. 12.— The number of narrow lines selected for OVI in artificial spectra with a spectrum cut by a factor of ten above 4 Ry, as described in §6.3. Agreement with Q1422 occurs for $Z \lesssim -2.9$.

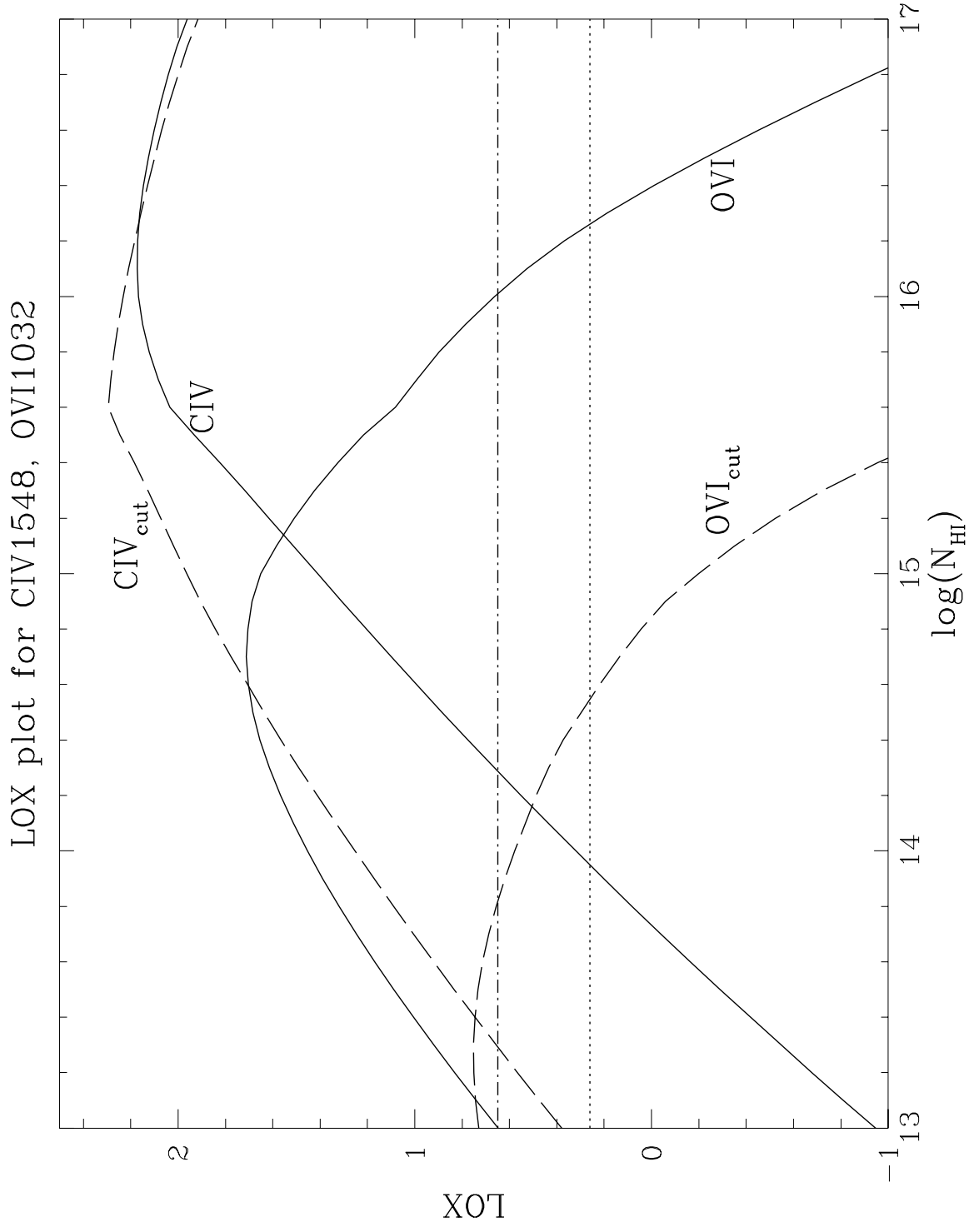
Fig. 13.— Histogram of $N_{\text{OVI,app}}/N_{\text{CIV}}$ in pixels associated with significant CIV absorption, as identified and measured by the optical depth ratio technique (§7.1). Solid line shows the results from six artificial spectra with [O/H] = -2.0 and [C/H] = -2.5, the dotted line shows the results from artificial spectra without oxygen, and the dashed histogram shows the results from Q1422.

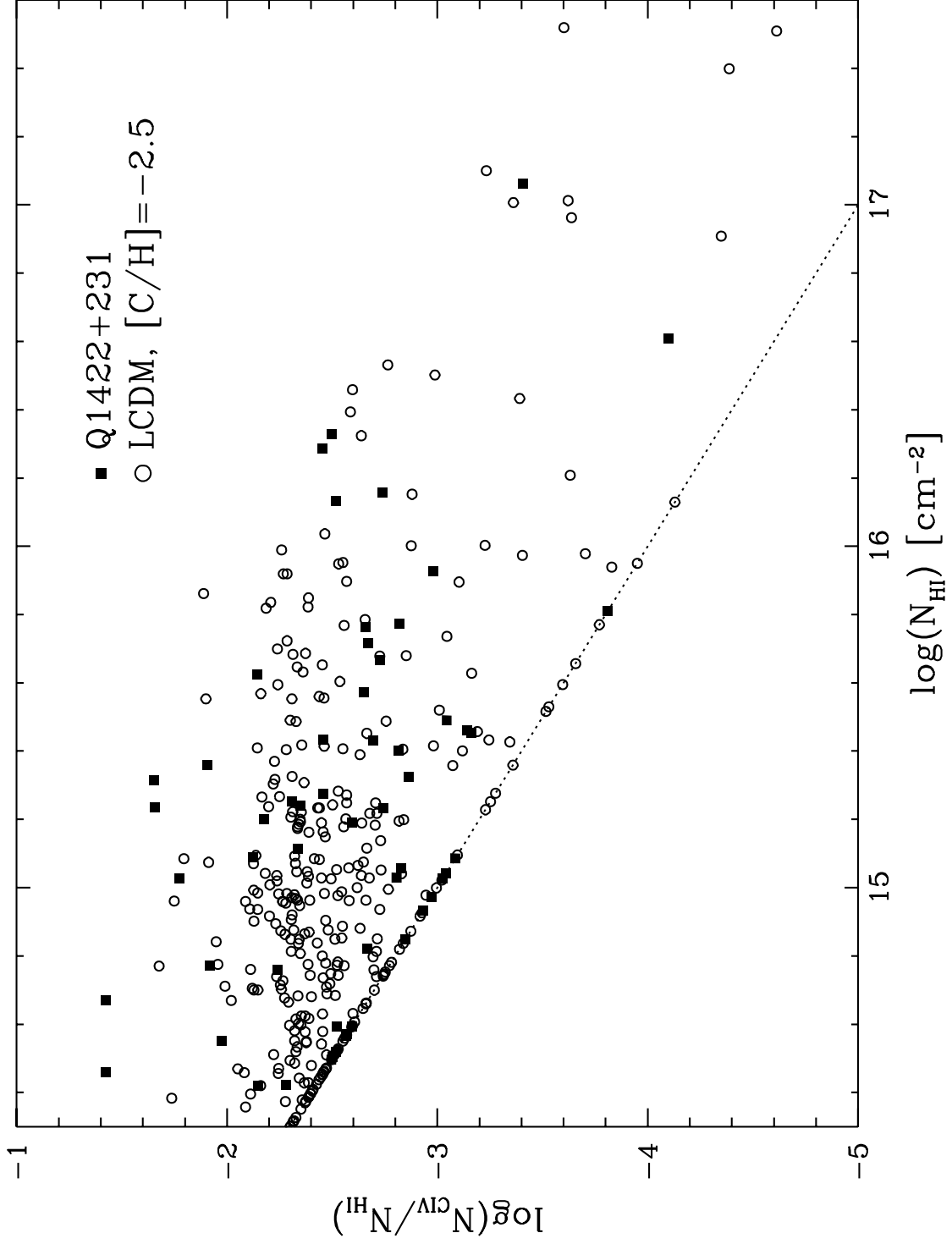
Fig. 14.— Median $N_{\text{OVI,app}}/N_{\text{CIV}}$ versus [O/H], with [C/H] held fixed at the value producing agreement with CIV data (solid line). The dashed line shows the Q1422 value of 8.3 while the dotted line shows the value from artificial spectra without oxygen (2.6). This confirms S98’s observation of a significant presence of OVI. The dot-dashed line shows the results from artificial spectra generated using the cut spectrum described in §6.3.

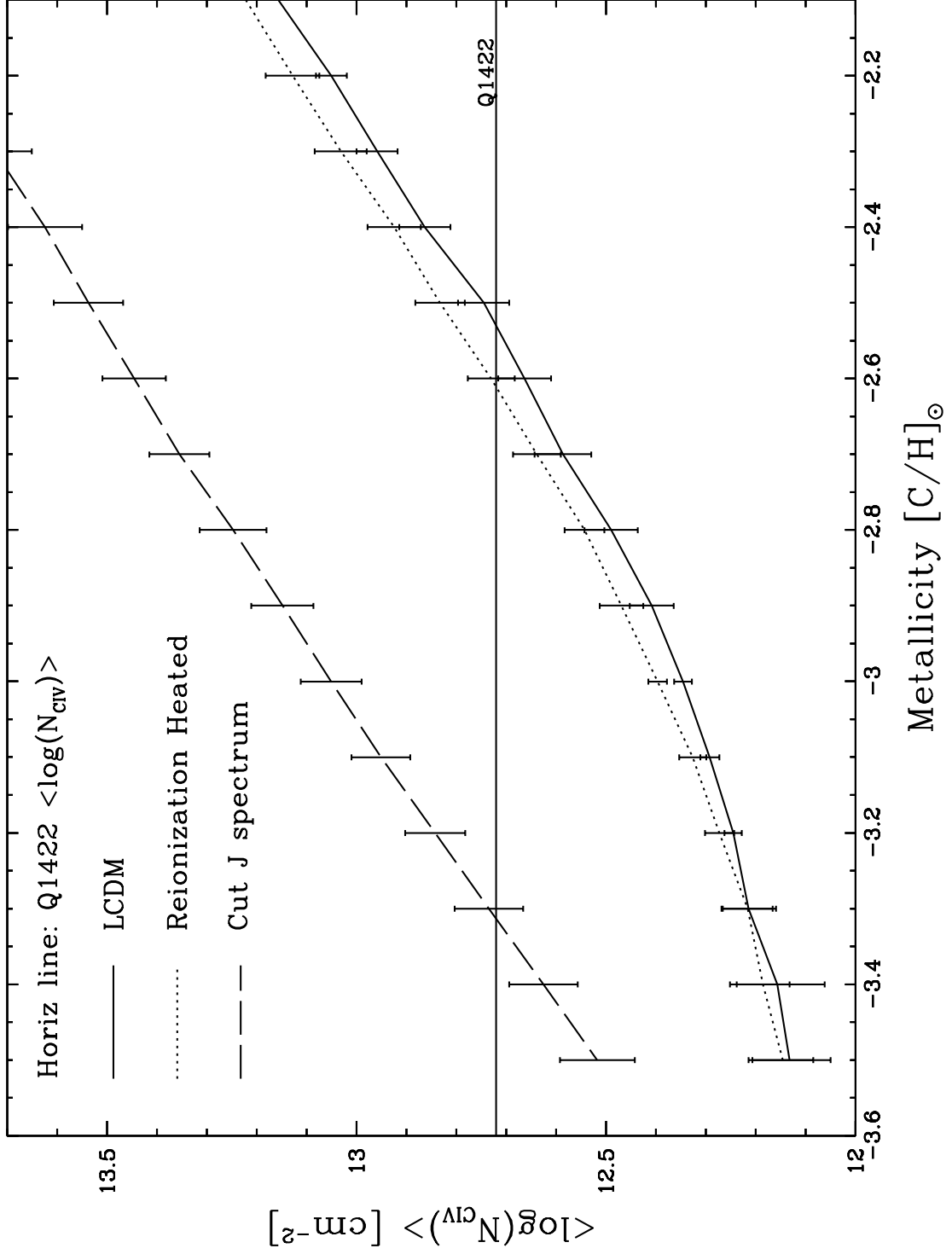


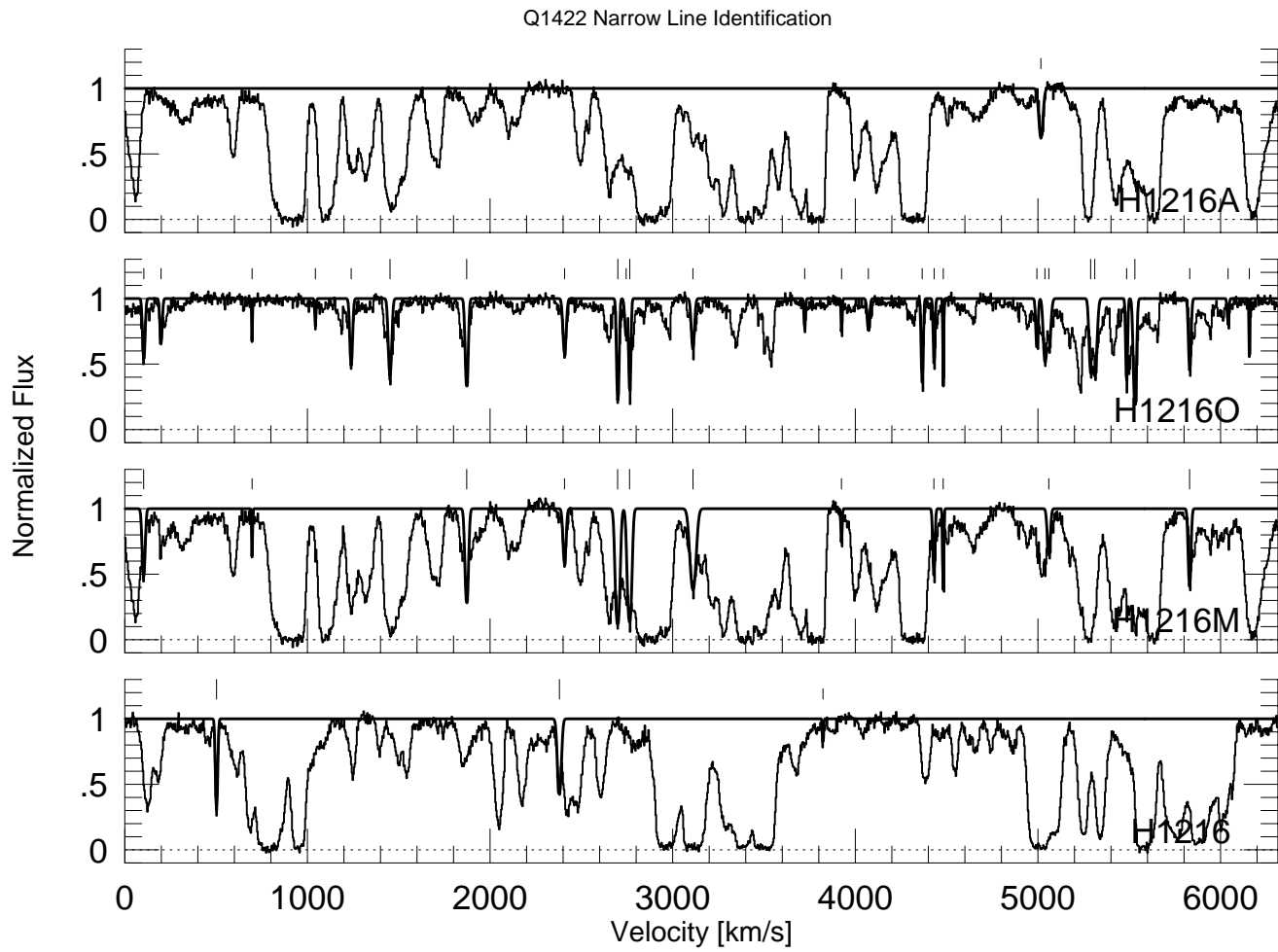
Q1422+231, Continuum Normalized

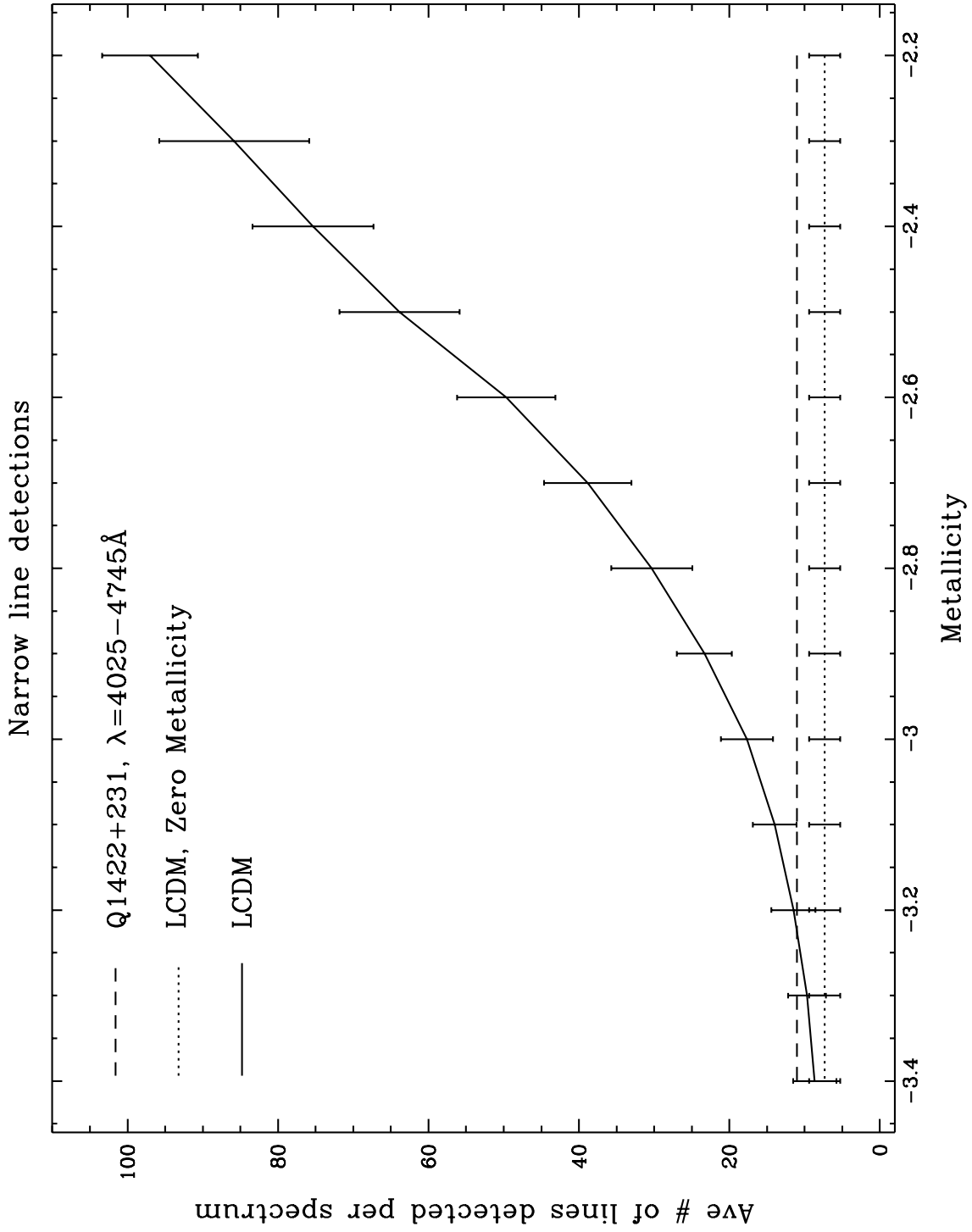
LCDM, $Z = -2.5$, Normalized, Noise Added

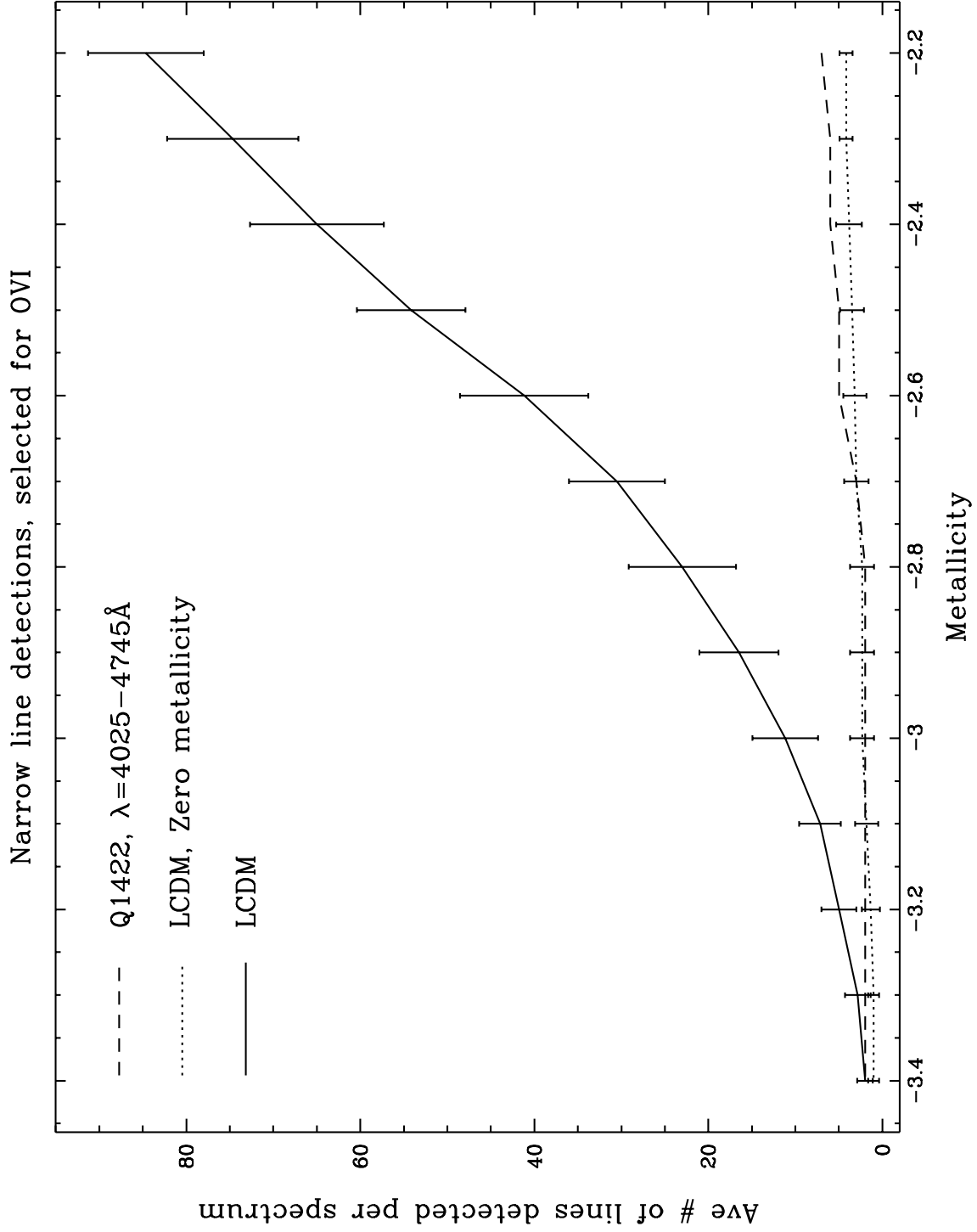


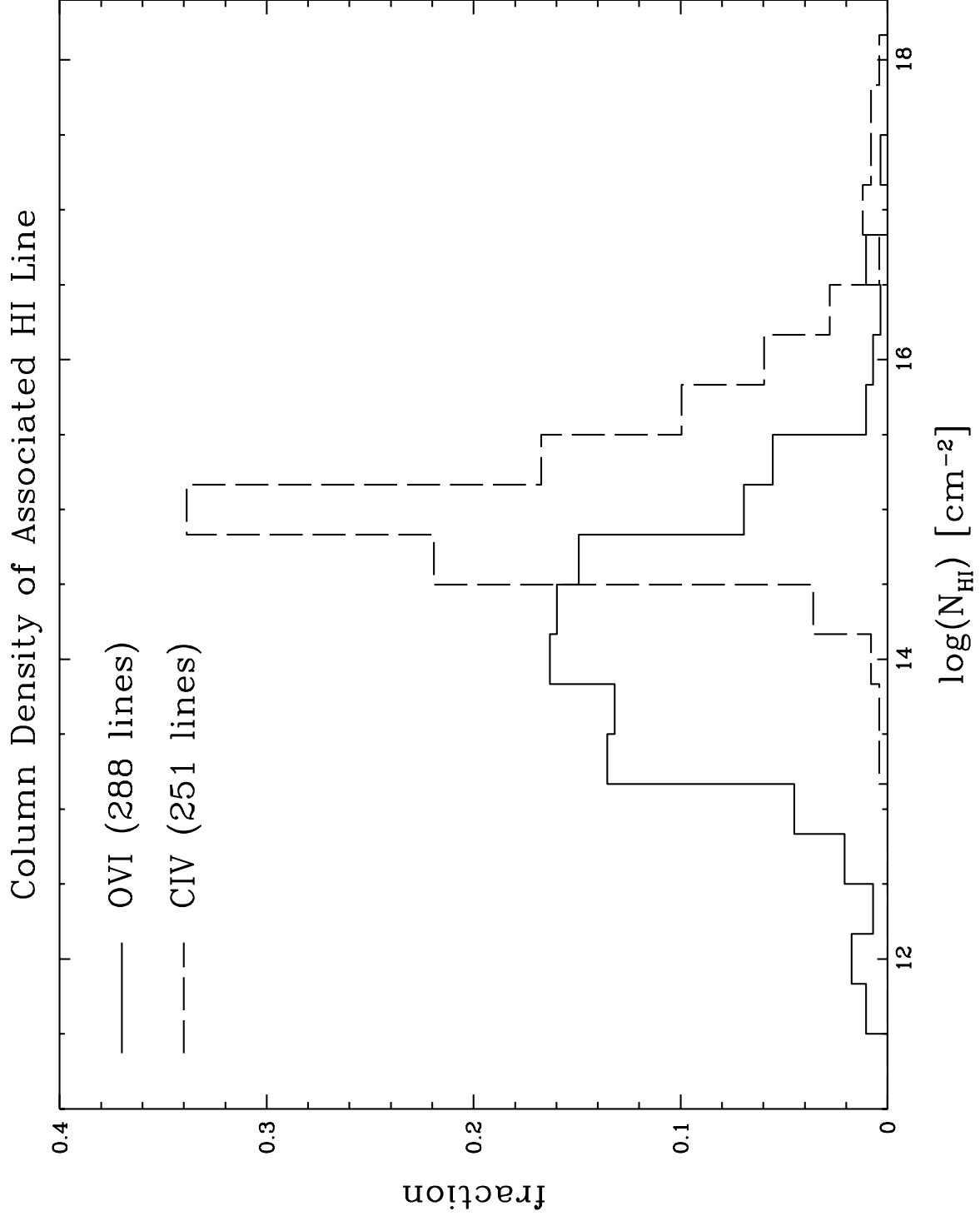




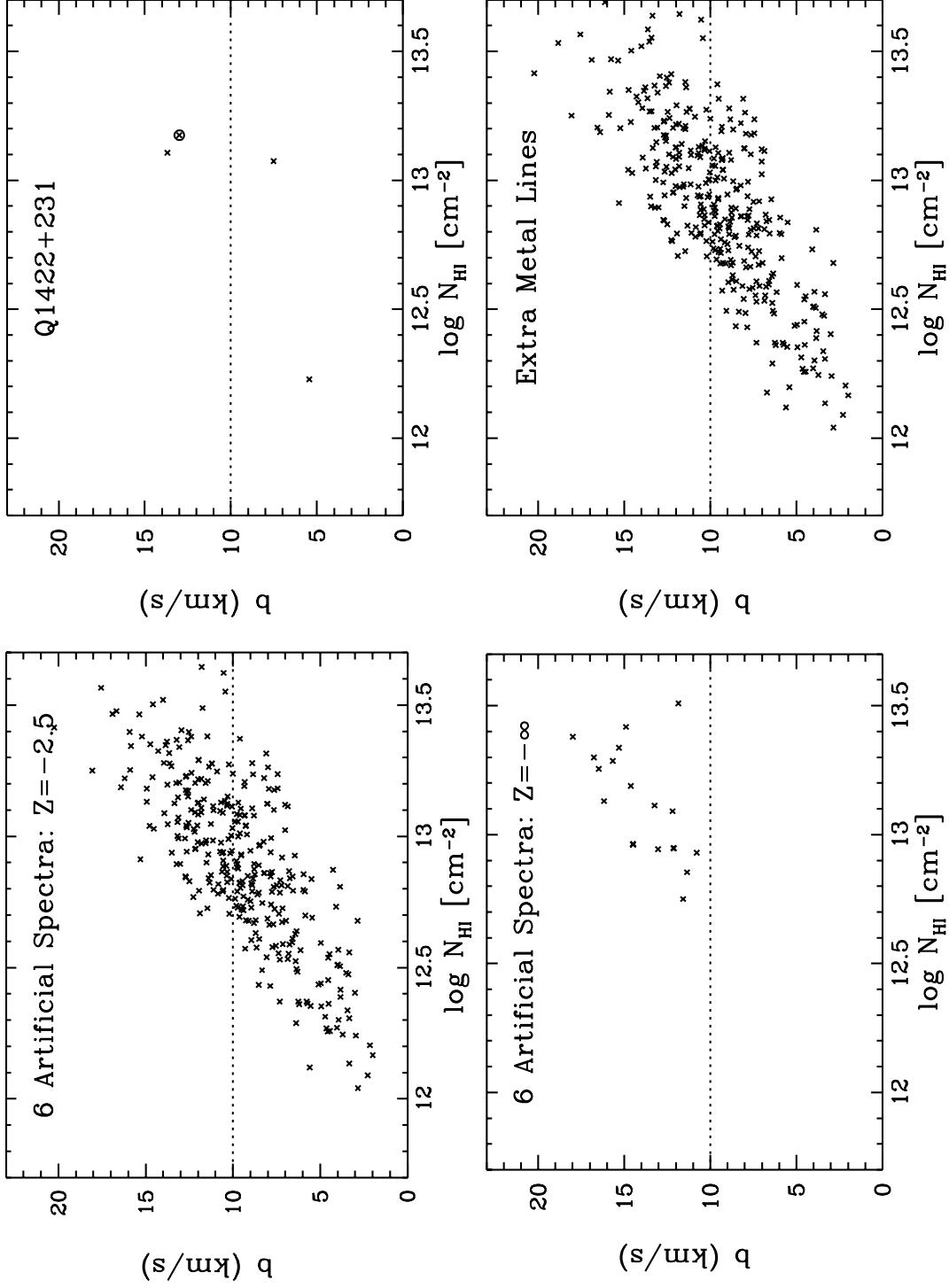




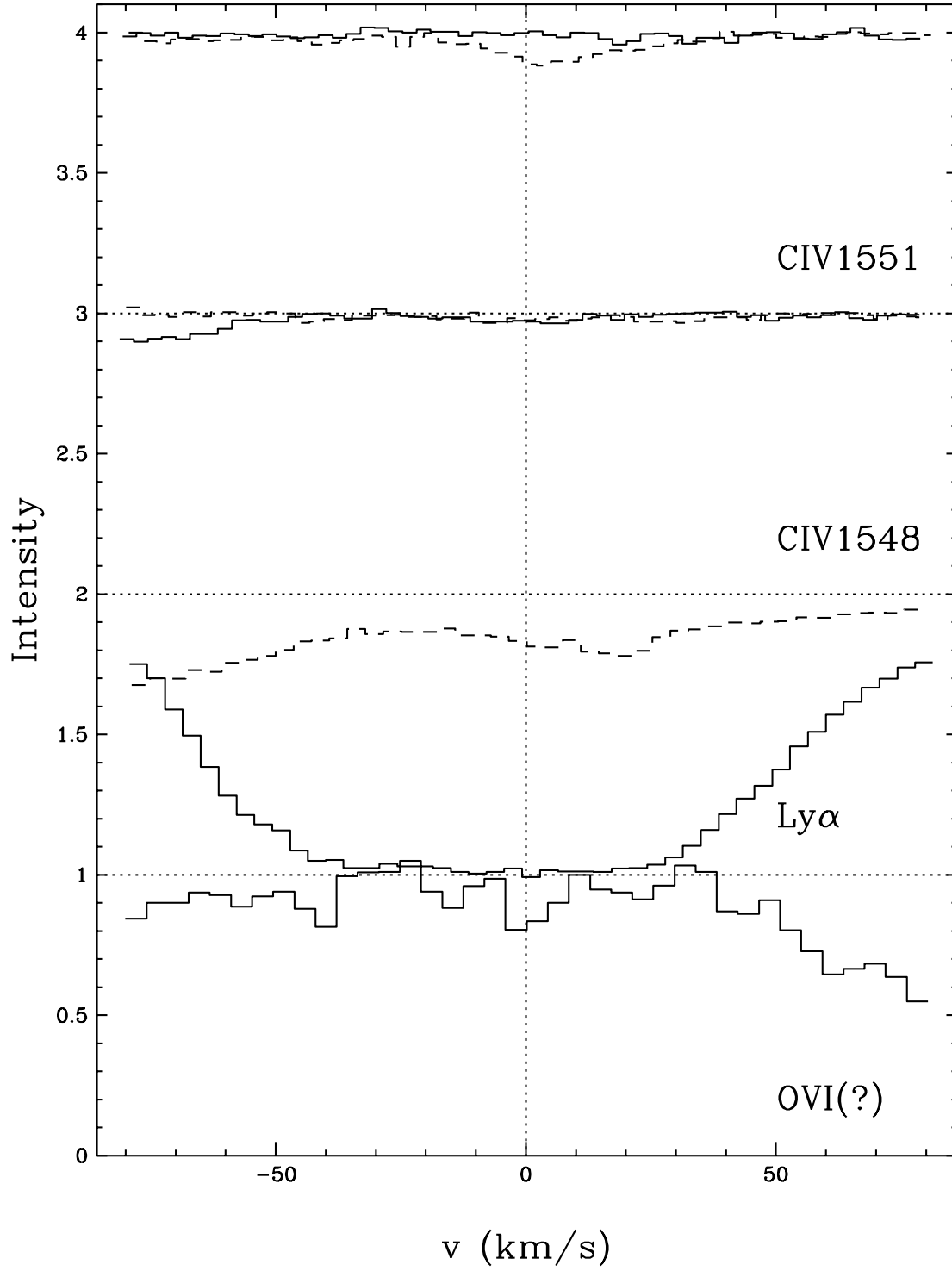




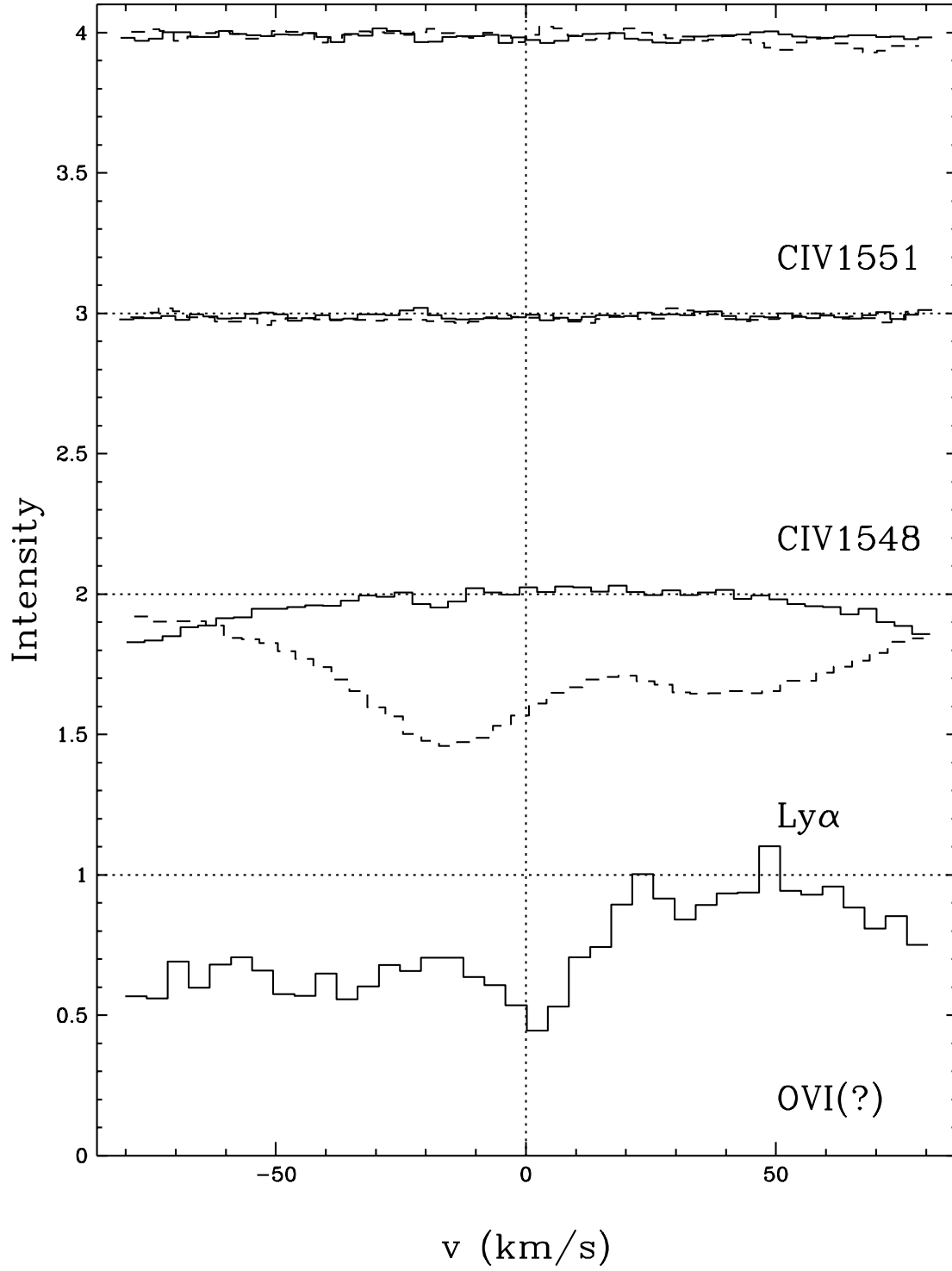
N_{HI} vs. b for Narrow Lines



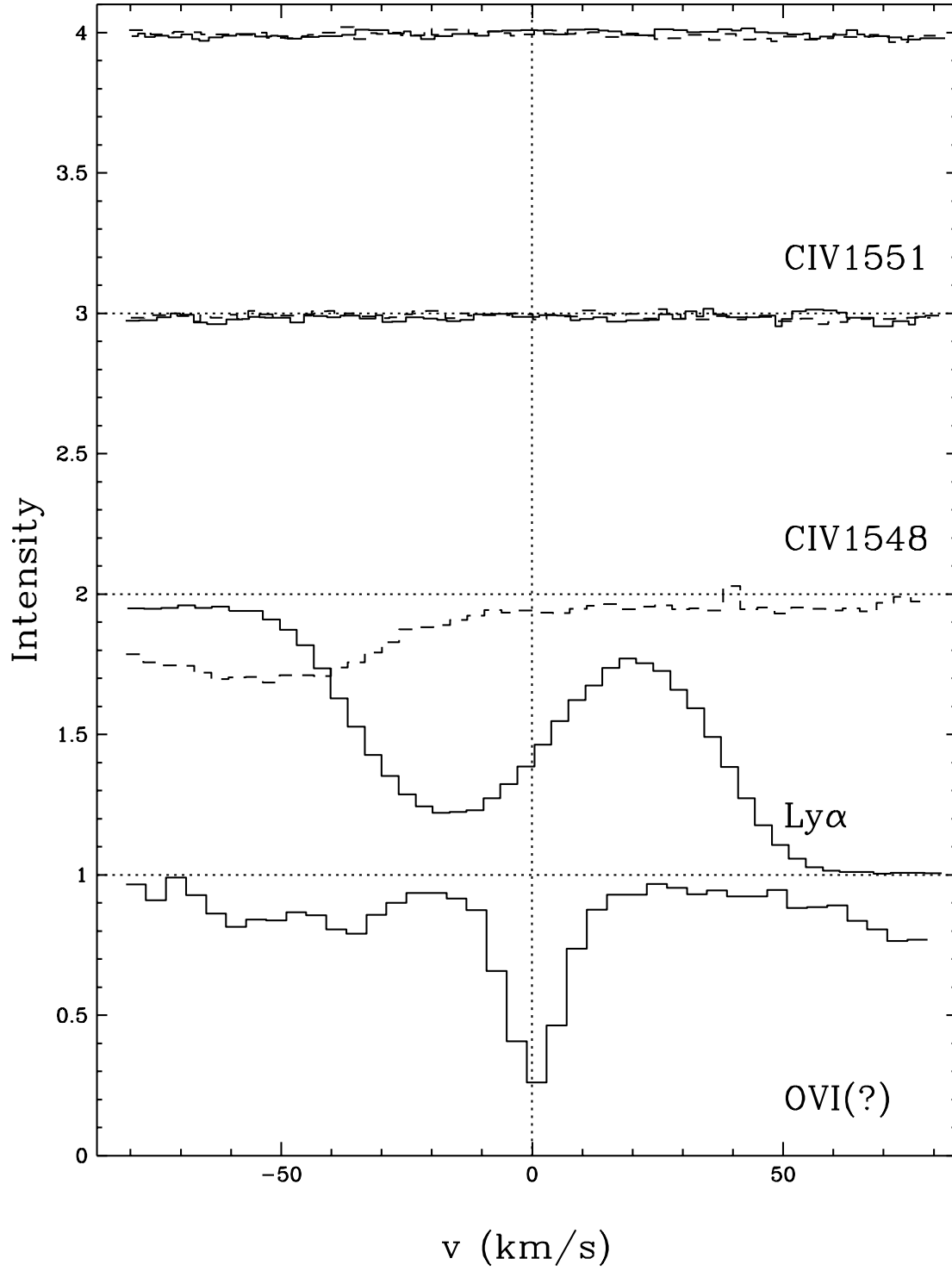
OVI System in Q1422 at 4276.497\AA ($b=5.443$)



OVI System in Q1422 at 4278.899Å (b=13.687)



OVI System in Q1422 at 4517.232\AA ($b=7.523$)



OVI System in Q1422 at 4545.453Å (b=12.987)

